Electronic structure and quantum transport in disordered graphene

Zi Wang
Centre for the Physics of Materials
Department of Physics
McGill University
Montréal, Québec
Canada

A Thesis submitted to the
Faculty of Graduate Studies and Research
in partial fulfillment of the requirements for the degree of
Master of Science

CONTENTS

List of Figures

Abstract

Graphene, a single sheet of graphite, has many interesting electronic and mechanical properties, making it a viable candidate for tomorrow's electronics. It remains the most widely studied material in condensed matter physics as of 2011. Due to various disorder effects, many useful properties of pristine graphene predicted by theory may not show up in real world systems, and the exact effects of disorder on graphene nanoelectronics have not been investigated to any satisfaction. The research goal of this thesis is to provide first principles calculations to study disorder scattering in graphene nanostructures.

We shall briefly review the basic concepts of electronic structure theory of condensed matter physics, followed by a more detailed discussion on density functional theory (DFT) which is the most widely applied atomistic theory of materials physics. We then present the LMTO implementation of DFT specialized in calculating solid crystals. LMTO is computationally very efficient and is able to handle more than a few thousand atoms, while remaining reasonably accurate. These qualities make LMTO very useful for analysing quantum transport. We shall then discuss applying DFT within the Keldysh non-equilibrium Green's function formalism (NEGF) to handle non-equilibrium situations such as current flow. Finally, within NEGF-DFT, we shall use the coherent potential approximation (CPA) and the non-equilibrium vertex correction (NVC) theory to carry out configurational disorder averaging.

This theoretical framework is then applied to study quantum transport in graphene with atomistic disorder. We shall investigate effects of substitutional boron (B) and nitrogen (N) doping in a graphene device connected to intrinsic graphene electrodes. We have calculated quantum transport of two-probe graphene devices versus disorder concentration x, device length L, electron electron energy E, and our results suggest that doping greatly affects quantum transport properties by inducing significant diffusive scattering.

In particular, it is the first time in literature that conductance versus doping concentration x is obtained from atomic first principles. Importantly, the NVC theory allows us to directly determine the diffusive scattering contribution to the total con-

ductance. Since B and N atoms are located on either side of carbon in the periodic table, a very interesting finding is that disorder scattering due to these impurities are mirrored almost perfectly on either side of the graphene Fermi level. Such a behavior can be understood from the point of view of charge doping.

Résumé

Le graphène, une seule feuille de graphite, a de nombreuse propriétés électroniques et mécaniques intéressantes, et ce qui en fait une solution viable pour l'électronique de demain. Il reste le matériau le plus largement étudié en physique de la matière condensée en 2011. En raison des effets du désordre, de nombreux propriétés utiles du graphène prédite par la théorie n'apparaissent pas dans les systèmes du monde réel, et les effets exacts du désordre dans le graphène n'ont pas été étudiées à toute satisfaction. L'objectif de cette thèse est de fournir une étude premiers principes de l'effet du désordre introduit dans des nanostructures de graphène.

Nous allons passer brièvement en revue les concepts de base de la théorie électronique de la matière condensée, suivie par une discussion plus détaillée sur la théorie de la fonctionnelle de la densité (DFT) qui est la théorie atomique la plus couramment appliquée pour la physique matériaux. Nous allons ensuite présenter la méthode LMTO, des de la DFT, qui est spécialisée dans le calcul des cristaux solides. LMTO est mathématiquement très efficace et est en mesure de traiter plus de quelques milliers d'atomes, tout en restant raisonnablement précise. Ces qualités font que la méthode LMTO est très utile pour l'analyse du transport quantique. Nous discuterons ensuite l'application du DFT est dans le formalisme de la fonction non-équilibre de Green de Keldysh (NEGF) pour traiter les systèmes non-équilibre, tels que le courant de charge. Enfin, dans NEGF-DFT, nous allons utiliser l'approximation du potentiel cohérent (CPA) et la correction non-équilibre de vertex (NVC) afin d'appliquer la théorie de la moyenne du désordre de configuration.

Ce cadre théorique est ensuite appliquée à l'étude du transport quantique dans le graphène avec du désordre atomique. Nous allons étudier les effets de la substitution du bore (B) et de l'azote (N) dans le graphène connecté aux électrodes de graphène pure. Nous avons calculé le transport quantique des dispositifs de graphène en fonction de la concentration du désordre x, longueur du dispositif L, l'énergie E, et nos résultats suggèrent que le dopage affecte grandement les propriétés de transport quantique en induisant diffusion de maniere significante.

En particulier, ceci est la première fois que la conductance en fonction de la con-

centration du dopage x est obtenue à partir de théorie premiers principes atomiques. Il est important de noter que la théorie de la NVC nous permet de déterminer directement la contribution de la diffusion à la conductance totale. Étant donné que les atomes B et N les atomes sont situés de chaque côté du carbone dans le tableau périodique, il est intéressant de constater que la diffusion du désordre due à ces impuretés apparait presque parfaitement de chaque côté du niveau de Fermi dans le graphène. Un tel comportement peut être compris du point de vue de la charge des dopants.

Acknowledgements

First and foremost, I would like to express the deepest gratitude to my supervisor, Prof. Hong Guo who has helped me through every step of my M.Sc. Not only is he always greatly motivated about science and research, his excellent wit and humour have been a great inspiration to me. His matter-of-fact views on both the scientific world and the real world has given me great insights on how to succeed in academics and beyond.

I would also like to give my sincere thanks to the members of our group, some of them already gone in pursuit of greatness, and all of them being exceptionally insightful and always very friendly and helpful. Particularly, I would like to thank Youqi Ke, Jesse Maasen, and Dongping Liu for always being there whenever I was stuck and needed help on both technical issues and understanding of the theory. Not only will I not forget your contributions to my research, I have also enjoyed our personal interactions very much.

I would like to acknowledge The Professor for reading and correcting my thesis in meticulous detail. Everything you said was very sharp and absolutely correct and has made my thesis that much better of a read.

Finally, I would like to thank my family and friends for their support during my career as a M.Sc. student here at McGill. McGill is a wonderful school and I have had a great albeit short two years being a McGill master's student. My experience here has given me important lessons on life and despite having been here for just two years, I know that this experience will leave me a lasting impression.

Physical Constants and Units

1 Å = 10^{-10} m

a_0 (Bohr radius) = 0.5292 Å

m_e (electron mass) = 9.1096×10^{-31} kg

m_p (proton mass) = 1.6726×10^{-27} kg

e (electron charge) = 1.6×10^{-19} C

h (Planck's constant) = 6.626×10^{-34} J s

k_B (Boltzmann's constant) = 1.38×10^{-23} K

k_BT (at 1 K) = 8.616×10^{-5} eV

c (speed of light) = 2.9979×10^{8} m/s

G_0 (quantum unit of conductance) = $7.75 \times 10^{-5}\Omega^{-1} = \frac{1}{12.9\text{k}\Omega}$

Atomic units are used throughout this thesis unless otherwise indicated. In this system of units, $e = m_e = \hbar = 1$.

1 unit of Length = a_0 = 0.5292 Å

1 unit of Mass = m_e = 9.1096×10^{-31} kg

1 unit of Charge = e = 1.6×10^{-19} C

1 unit of Angular momentum = $\hbar$ = 1.0546×10^{-34} J s

1 unit of Energy = 1 Hartree = 27.2 eV

1 unit of Time = $\frac{\hbar}{1\ \text{Hartree}}$ = 2.4189×10^{-17} s

List of Abbreviations

SE	Schrödinger's Equation
TISE	Time Independent Schrödinger's Equation
DFT	Density Functional Theory
NEQ	Non-Equilibrium
NEGF	Non-Equilibrium Green's Function
NVC	Non-Equilibrium Vertex Correction
CPA	Coherent Potential Approximation
LDA	Local Density Approximation
LMTO	Linear Muffin Tin Orbital
ASA	Atomic Sphere Approximation
BZ	Brillouin Zone

1

Introduction

Carbon is a nonmetallic tetravalent element. Because it has four electrons available to make covalent bonds, it is highly flexible in its bonding and is able to form more compounds than any other element, all with large varieties of physical properties. Carbon is the basis for all life on earth and the main component in organic chemistry. Carbon itself occurs in several allotropes including amorphous carbon, diamond, and graphite, all having widely varying physical properties. Graphene, a single sheet of graphite, is another allotrope of carbon that has been recently isolated [7].

The dimensionality of the above mentioned carbon materials plays a very important role for their physical properties[8]. Graphene consists of carbon atoms arranged on a hexagonal honeycomb lattice and can be seen as an infinitely large aromatic molecule. Physically, it is a two-dimensional (2D) structure. This sheet of carbon can be warped by introducing pentagons on the hexagonal lattice, wrapping it up into a spherical configuration called fullerenes, a physically zero-dimensional (0D) object with discrete energy levels. Rolling up the sheet in a particular direction and reconnecting the bonds gives carbon nanotubes (1D) that have been the subject of extensive study for almost two decades. Stacking up sheets of graphene results in 3D graphite, the well known material in pencils, batteries, and other applications requiring a soft conducting material.

The remarkable properties of single layer graphite have been investigated theoretically since the Second World War [9, 10] but graphene has been considered a purely

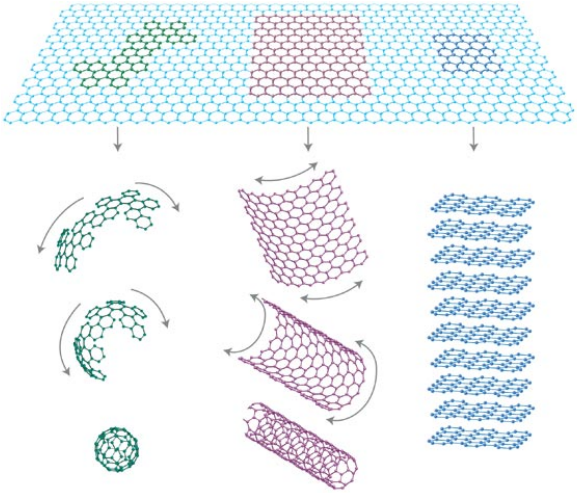

Figure 1.1: Taken from Ref.[1], this image shows how graphene can be used to build the other carbon structures. It can be wrapped up to produce 0D fullerene, rolled up into 1D nanotubes, or stacked to create 3D graphite.

theoretical material since it was believed that a single 2D layer would be thermodynamically unstable [11, 12] and would therefore not exist in an isolated state. After its experimental discovery [7], however, both theoretical and experimental research on the properties of graphene have taken off and have resulted in the 2010 Nobel Prize awarded to its discoverers, A. K. Geim and K. S. Novoselov. We will shortly list a few important features of graphene, and refer interested readers to more extensive reviews on this interesting material[1, 2, 13].

The most distinguishable electronic property of graphene is its linear dispersion relation near the K-points of the Brillouin zone predicted by tight binding calculations a long time ago[9]:

$$E_{\mathrm{TB}} = \pm\sqrt{\gamma_0^2\left(1 + 4\cos^2\frac{k_y a}{2} + 4\cos\frac{k_y a}{2}\cos\frac{k_x\sqrt{3}a}{2}\right)}, \tag{1.0.1}$$

where $\gamma_0 \approx 2.8\,\mathrm{eV}$ is the tight binding nearest-neighbour hopping energy, and $a \approx 2.46\,\text{Å}$ is the lattice constant. If we plot this (see Fig. 1.2), we can observe that near the K-points, the valence and conduction bands touch each other and the dispersion relation is linear to a good approximation. This implies that close to those points, the quasi-particle charge carriers have zero effective mass and therefore should be described by the massless Dirac's equation [2]. This feature alone makes it possible to study much interesting physics using graphene as a medium.

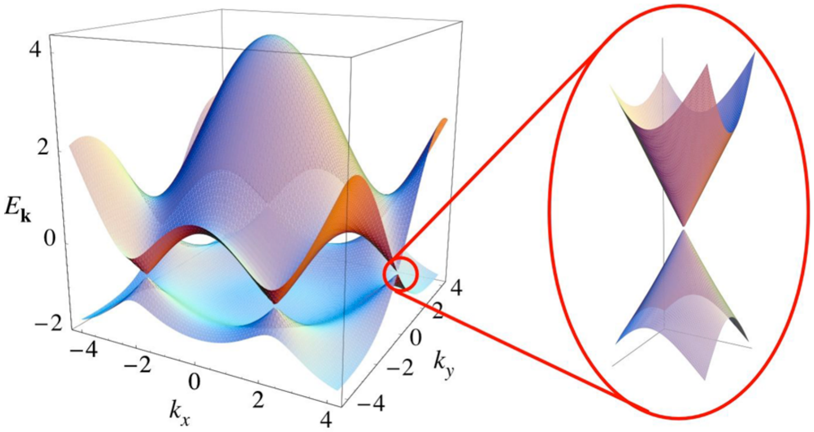

Figure 1.2: The dispersion relation of graphene [2]. Close to the K-points, the corners of the hexagonal Brillouin zone, the valence and conduction bands touch each other, and the dispersion relation is linear.

Another property of graphene is its high electron mobility even at room temperature, measured to be higher than $15,000\text{cm}^2\text{V}^{-1}\text{s}^{-1}$ [1]. This results in potentially very high conductivity of graphene. An extensively studied property of graphene is its anomalous quantum Hall effect[1]. Graphene also exhibits many interesting mechanical properties, but these will not be the scope of the present thesis.

Because of its properties, graphene has been touted as the potential new material to eventually replace silicon for use in nanoelectronics, including transistors and integrated circuits. It is this application that has enjoyed the most attention, and to achieve any practical applications in this direction, it is still required to conduct significant investigations on various electronic properties of graphene under different realistic circumstances. It is on these electronic properties that we will focus in this thesis.

Graphene itself can exist in many forms too, such as nanoribbons, bi- and trilayer graphene, and all of these forms exhibit different transport properties and all have potential applications in many different fields. There have been extensive studies conducted on all of those forms [14, 15].

From a theoretical point of view, it is important to investigate the quantum transport properties of graphene and predict how graphene acts in real situations with reasonable accuracy. So far, there has already been a considerable amount of studies on charge and spin transport in graphene using both empirical and first principles methods. It is an exhaustive exercise to refer to all of the important studies, so instead we will cite an excellent review paper [2] which covers most of the efforts done already.

An important issue to consider is that no material is arranged perfectly. Since experiments are done on materials with imperfections, the values they measure are often very different compared to the quantities predicted by theoretical models that usually do not take these imperfections into account. The challenge is thus how to incorporate these imperfections such as impurities and disorder in a theoretical model in order to make realistic predictions with reasonable accuracy. For graphene, these imperfections are considered to play an important role in determining its properties. None of the ab-initio theoretical studies however have had the ability to exhaustively generate the huge number of randomly disordered configurations and compute each of them for accurate statistical averaging of results. Usually only a small number of configurations are sampled (if at all), limiting the applicability of their results.

In this thesis, we will start with a short introduction to electronic structure theory in condensed matter physics. This is followed by a review on density functional theory (DFT), the most widely used computational approach in condensed matter physics, materials science, quantum chemistry, biology and various disciplines of engineering. Chapter 3 presents the linearized Muffin-Tin orbital (LMTO) method which is a particular implementation of DFT. LMTO is highly efficient for calculations on solid crystals. Then, in Chapter 4, we will briefly review the non-equilibrium Green's function formalism (NEGF) for quantum transport, and a method where DFT is carried out within NEGF so that non-equilibrium quantum transport problems in open device structures can be solved from atomic first principles. Within the framework of NEGF-DFT, we will outline the main theoretical tool used in this thesis for calculating disorder scattering, namely the coherent potential approximation (CPA) and the non-equilibrium vertex correction (NVC) theory. This is a recently developed formalism [16, 17] which enables us to handle disordered systems and calculate their transport properties from NEGF-DFT first principles methods.

The original research in this thesis, which will be published in a peer-reviewed journal [18], is to apply the NEGF-DFT first principles method to investigate quantum transport in graphene with atomistic disorder. This work is the content of Chapter 5. We shall investigate effects of substitutional boron (B) and nitrogen (N) doping in a graphene device connected to intrinsic graphene electrodes. We have calculated quantum transport of two-probe graphene devices versus the disorder concentration x, the device length L, the electron electron energy E, and our first principles results suggest that impurity doping greatly affects quantum transport properties by inducing significant diffusive scattering. In particular, it is the first time in literature that conductance versus doping concentration x is obtained from atomic first principles. Importantly, the NVC theory will allow us to directly determine the diffusive scattering contribution to the total conductance.

2

Electronic Structure Theory

2.1 The Schrödinger equation

Condensed matter phenomena are usually described by a Hamiltonian that accounts for most of the relevant physics yet can be written down in just a single line:

$$\hat{\mathcal{H}} = -\frac{1}{2}\sum_{l}\frac{\nabla_l^2}{M_l} + \frac{1}{2}\sum_{l\neq l'}\frac{q_l q_l'}{|\mathbf{r}_l - \mathbf{r}_{l'}|}, \tag{2.1.1}$$

where $\mathbf{r}_l$ are the positions, M_l the mass and q_l the charge of the electrons or nuclei. The sums range over all electrons and nuclei of the solid. The contributions to the potential (the second term in Eq. 2.1.1) by the electrons and nuclei can be written down separately, so we define below the kinetic energy terms $\hat{T}_e$ and $\hat{T}_n$ for the electrons and nuclei, respectively, and the potential terms $\hat{V}_{ee}$, $\hat{V}_{nn}$, $\hat{V}_{ext}$ of the electron-electron, nucleus-nucleus and electron-nucleus interactions,

$$\hat{T}_e = -\frac{1}{2}\sum_{i}\nabla^2(\mathbf{r}_i), \tag{2.1.2}$$

$$\hat{T}_n = -\frac{1}{2}\sum_{i}\frac{1}{M_i}\nabla^2(\mathbf{R}_i), \tag{2.1.3}$$

$$\hat{V}_{ee} = \frac{1}{2}\sum_{i\neq j}\frac{1}{|\mathbf{r}_i - \mathbf{r}_j|},, \tag{2.1.4}$$

$$\hat{V}_{nn} = \frac{1}{2}\sum_{i\neq j}\frac{Z_i Z_j}{|\mathbf{R}_i - \mathbf{R}_j|}, \tag{2.1.5}$$

$$\hat{V}_{ext} = -\sum_{i,j}\frac{Z_j}{|\mathbf{r}_i - \mathbf{R}_j|}. \tag{2.1.6}$$

$\nabla^2(\mathbf{r}_i)$ means that the Laplacian only applies to $\mathbf{r}_i$ which represents the position of an electron, M_i, Z_i, $\mathbf{R}_i$ represent the mass, atomic number and position of a nucleus. The Hamiltonian (2.1.1) becomes a sum of these terms:

$$\hat{\mathcal{H}} = \hat{T}_e + \hat{T}_n + \hat{V}_{ee} + \hat{V}_{nn} + \hat{V}_{ext}. \tag{2.1.7}$$

To solve the corresponding Schrödinger equation (SE) for a three dimensional system of M nuclei and N electrons, one needs to deal with a many-body problem where a wavefunction Ψ depends on $3(M+N)$ spatial degrees of freedom plus the corresponding spin degrees of freedom. For very small systems, *i.e.* the few-body problem, it is possible to accurately solve the Schrödinger equation for the Hamiltonian (2.1.7) on a modern computer. However, studying actual macroscopic solids having $\sim 10^{23}$ atoms requires many levels of approximations.

2.1.1 The Born-Oppenheimer approximation

To make the Hamiltonian (2.1.7) more manageable for larger systems than just a few electrons, it is noted that the mass of an electron is far smaller than that of a nuclei. Therefore it is sensible to break up the wavefunction into its electronic and nuclear components:

$$\Psi_{\text{total}} = \Psi_{\text{electronic}} \times \Psi_{\text{nuclear}}, \tag{2.1.8}$$

and solve the Schrödinger equation in two steps. In the first step, the positions of the nuclei are held fixed and the electronic Schrödinger equation is solved with the nuclei acting as an external potential. In this way, wave functions for the electrons are in principle obtained. In the second step, the electronic wave functions are used to build a potential and force field for the nuclei so that the Schrödinger equation for the nuclei can be solved. This process is iterated until both the electronic and nuclear degrees of freedom are determined. Solving for the electronic wave function in a *fixed* nuclear potential landscape is the Born-Oppenheimer approximation. Of course, if the nuclear dynamics are not needed, the nuclei will just provide a potential for the electrons.

Since most electronic structure theory in solid state physics is based on the Born-Oppenheimer approximation, Eq. (2.1.1) is written in the following form:

$$\hat{\mathcal{H}} = \left[-\frac{1}{2} \sum_i \nabla_i^2 - \sum_{i,j} \frac{Z_j}{|\mathbf{r}_i - \mathbf{R}_j|} + \frac{1}{2} \sum_{i \neq j} \frac{1}{|\mathbf{r}_i - \mathbf{r}_j|} \right] . \tag{2.1.9}$$

The time independent Schrödinger equation (TISE), $\hat{\mathcal{H}}\Psi = \mathcal{E}\Psi$, now depends on a many-electron wave function depending on $3N$ spatial and N spin variables,

$$\Psi = \Psi \left(\mathbf{r}_1, s_1, \mathbf{r}_2, s_2, \ldots, \mathbf{r}_N, s_N \right) \ . \tag{2.1.10}$$

While it is not the concern of this work, we note that the Born-Oppenheimer approximation may not be a very good approximation or may even break down when very light elements such as hydrogen are involved in small molecule chemical reactions. For those problems, unfortunately, the full many-body problem might have to be solved. In the rest of this work which will focus on quantum transport in carbon nanostructures, the Born-Oppenheimer approximation is well justified and will be applied throughout.

2.2 The electron gas

A good starting point for solids [19, 20] is to consider an interacting electron gas moving in a background of positively charged ions (an application of the Born-

Oppenheimer approximation). This is especially a good model for most metals. Since it is still impossible to calculate interactions between $\sim 10^{23}$ electrons, further approximations are needed. The simplest zero-order approximation is to neglect the electron-electron interaction altogether, hence considering a non-interacting electron gas. With the ions held static, the Hamiltonian of this system becomes:

$$\hat{\mathcal{H}} = \sum_i \left[-\frac{1}{2}\nabla_i^2 - V_{ext}(\mathbf{r}_i) \right], \qquad (2.2.1)$$

with V_{ext} the external potential provided by the static ions. For solids containing 10^{23} atoms, the potential V_{ext} is still far too complicated to solve, but luckily there are further approximations one can make.

2.2.1 Bloch's theorem

For crystal solids, the ions are arranged in a periodic lattice, hence the potential V_{ext} must also be periodic, namely:

$$V(\mathbf{r}+\mathbf{R}) = V(\mathbf{r}) \qquad (2.2.2)$$

for any lattice vector $\mathbf{R}$. To study periodic behavior it is useful to study the Fourier transform of periodic functions. The positions $\mathbf{R}$ of the ions in the lattice can be written in terms of the lattice basis vectors $\{\mathbf{a}_1, \mathbf{a}_2, \mathbf{a}_3\}$ as

$$\mathbf{R} = n_1\mathbf{a}_1 + n_2\mathbf{a}_2 + n_3\mathbf{a}_3, \qquad n_1, n_2, n_3 \in \mathbb{Z}. \qquad (2.2.3)$$

By Fourier transforming from the real space, a reciprocal $\mathbf{k}$-space is defined using all the reciprocal lattice vectors,

$$\mathbf{G} = m_1\mathbf{b}_1 + m_2\mathbf{b}_2 + m_3\mathbf{b}_3, \qquad m_1, m_2, m_3 \in \mathbb{Z}\ , \qquad (2.2.4)$$

where the reciprocal lattice vectors $\mathbf{G}$ satisfies the relation $e^{i\mathbf{G}\cdot\mathbf{R}} = 1$; and the reciprocal basis vectors $\{\mathbf{b}_1, \mathbf{b}_2, \mathbf{b}_3\}$ are defined as

$$\mathbf{b}_1 = 2\pi\frac{\mathbf{a}_2 \times \mathbf{a}_3}{\mathbf{a}_1 \cdot \mathbf{a}_2 \times \mathbf{a}_3}, \quad \mathbf{b}_2 = 2\pi\frac{\mathbf{a}_3 \times \mathbf{a}_1}{\mathbf{a}_2 \cdot \mathbf{a}_3 \times \mathbf{a}_1}, \quad \mathbf{b}_3 = 2\pi\frac{\mathbf{a}_1 \times \mathbf{a}_2}{\mathbf{a}_3 \cdot \mathbf{a}_1 \times \mathbf{a}_2}. \tag{2.2.5}$$

The concept of Brillouin zones (BZ) is analogous to that of Wigner-Seitz cells in real space, and especially the first Brillouin zone (FBZ) plays an important role in solid state physics. It is defined as all $\mathbf{k}$ in $\mathbf{k}$-space lying closer to $\mathbf{G} = 0$ than to any other reciprocal lattice vector $\mathbf{G} \neq 0$. Any other vector $\mathbf{q}$ can thus be decomposed into the part $\mathbf{k}$ inside the FBZ and a lattice vector $\mathbf{G}$: $\mathbf{q} = \mathbf{k} + \mathbf{G}$.

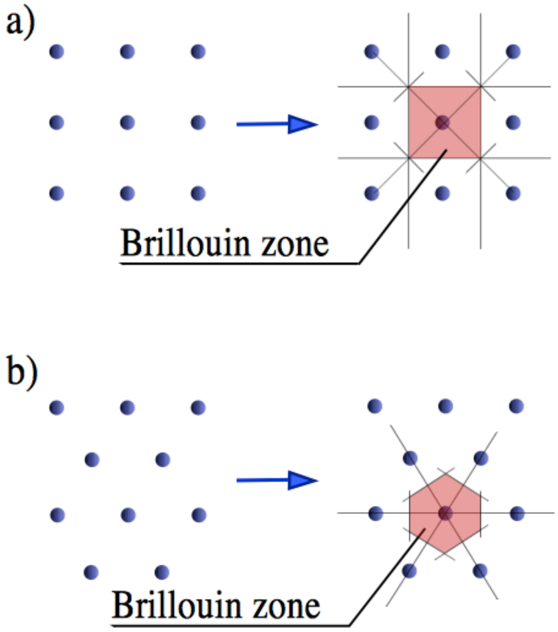

Figure 2.1: A schematic drawing taken from Ref. [3] of the construction of Brillouin zones for (a) square lattices and (b) hexagonal lattices, analogous to that of Wigner-Seitz cells. Any vectors $\mathbf{q}$ can thus be mapped inside the first Brillouin zone with a combination of $\mathbf{k}$ inside the FBZ and a lattice vector $\mathbf{G}$: $\mathbf{q} = \mathbf{k} + \mathbf{G}$.

Using the crystal periodicity of the potential (2.2.2), we can formulate an expression for the wave function:

$$\hat{\mathcal{H}}\psi_{n\mathbf{k}} = \mathcal{E}_{n\mathbf{k}}\psi_{n\mathbf{k}}, \qquad \psi_{n\mathbf{k}}(\mathbf{r}) = e^{i\mathbf{k}\cdot\mathbf{r}}u_{n\mathbf{k}}(\mathbf{r}), \tag{2.2.6}$$

where $\mathbf{k} \in \mathrm{FBZ}$, n is called the band index, $e^{i\mathbf{k}\cdot\mathbf{r}}$ is the plane wave envelope function and $u_{n\mathbf{k}}(\mathbf{r})$ is the Bloch amplitude which is periodic in the lattice. The second equation in (2.2.6) is Bloch's theorem.

Inserting the wavefunction of (2.2.6) into the Schrödinger equation, we obtain the equation for $u_{n\mathbf{k}}(\mathbf{r})$,

$$\hat{\mathcal{H}}_{\mathbf{k}} u_{n\mathbf{k}}(\mathbf{r}) = \frac{1}{2}\left[-\nabla^2 - 2i\mathbf{k}\cdot\nabla + k^2\right] u_{n\mathbf{k}}(\mathbf{r}) + V(\mathbf{r}) u_{n\mathbf{k}}(\mathbf{r}) = \mathcal{E}_{n\mathbf{k}} u_{n\mathbf{k}}(\mathbf{r}). \qquad (2.2.7)$$

Due to periodicity of $u_{n\mathbf{k}}(\mathbf{r})$, we can solve equation (2.2.7) in just the first Brillouin zone with periodicity and smoothness as boundary conditions:

$$u_{n\mathbf{k}}(\mathbf{r}) = u_{n\mathbf{k}}(\mathbf{r}+\mathbf{R}), \qquad (2.2.8a)$$

$$\hat{n}(\mathbf{r})\cdot\nabla u_{n\mathbf{k}}(\mathbf{r}) = -\hat{n}(\mathbf{r}+\mathbf{R})\cdot\nabla u_{n\mathbf{k}}(\mathbf{r}+\mathbf{R}), \qquad (2.2.8b)$$

or, in terms of $\psi_{n\mathbf{k}}(\mathbf{r})$,

$$e^{i\mathbf{k}\cdot\mathbf{R}}\psi_{n\mathbf{k}}(\mathbf{r}) = \psi_{n\mathbf{k}}(\mathbf{r}+\mathbf{R}), \qquad (2.2.9a)$$

$$e^{i\mathbf{k}\cdot\mathbf{R}}\hat{n}(\mathbf{r})\cdot\nabla\psi_{n\mathbf{k}}(\mathbf{r}) = -\hat{n}(\mathbf{r}+\mathbf{R})\cdot\nabla\psi_{n\mathbf{k}}(\mathbf{r}+\mathbf{R}). \qquad (2.2.9b)$$

The problem of solving for a crystal of $\sim 10^{23}$ atoms has now been reduced to one that requires solving just the first Brillouin zone.

2.2.2 The jellium model

Even though Eq. (2.2.7) has been reduced to just the FBZ by virtue of Bloch's theorem, it is still too hard to solve analytically. A somewhat simple analytical formulation can be done if one uses the so called jellium model of metals. The jellium model assumes that the ionic charges are *uniformly* spread out in the entire volume of the solid. This crude approximation removes the nuclei of the atoms altogether and makes the free electron problem solvable. It is an unrealistic description but has great theoretical significance in the development of modern electronic structure theory for solids. We shall discuss this model here and in this section, SI units will be used.

Ignoring electron-electron interactions, the Hamiltonian reduces to a simple form consisting only of the kinetic energy term:

$$\hat{\mathcal{H}}_{jel} = \hat{T}_e = -\frac{\hbar^2}{2m}\sum_i \nabla_i^2. \tag{2.2.10}$$

This is the problem of many non-interacting particles in a box, where the single particle states are given by

$$\hat{\mathcal{H}}_{jel}\psi_{\mathbf{k}} = \frac{\hbar^2 k^2}{2m}\psi_{\mathbf{k}}, \quad \psi_{\mathbf{k}}(\mathbf{r}) = \frac{1}{\sqrt{\mathcal{V}}}e^{i\mathbf{k}\cdot\mathbf{r}}, \quad \begin{cases} k_x & = \frac{2\pi}{L_x}n_x \quad (\text{for } x,\, y \text{ and } z), \\ n_x & = 0, \pm 1, \pm 2, \ldots, \\ \mathcal{V} & = L_x L_y L_z. \end{cases} \tag{2.2.11}$$

The quantization of **k** gives a volume of $\frac{(2\pi)^3}{\mathcal{V}}$ for every state in **k**-space. This is of great help, since we can take integrals as limits of sums over **k**-space normalized by this volume and obtain the relation

$$\sum_{\mathbf{k}} \longrightarrow \frac{\mathcal{V}}{(2\pi)^3}\int \mathrm{d}\mathbf{k}. \tag{2.2.12}$$

The ground state for N electrons is denoted by $|\, FS\,\rangle$ and is obtained by filling up **k**-space with the N lowest possible energies according to the E-**k** dispersion relation for free electrons, $E(\mathbf{k}) = \frac{\hbar^2 k^2}{2m}$. In **k**-space, these states will fill up a sphere called the Fermi sphere (Fig. 2.2), where all states $\mathcal{E}_{\mathbf{k}} < \mathcal{E}_F$ with momentum $k < k_F$ are occupied. The states above this energy are unoccupied, so all important physics take place at the surface of this sphere, the Fermi surface. There are several important quantities related to this Fermi surface, such as the Fermi wavenumber k_F, the Fermi wavelength λ_F, and the Fermi velocity v_F. Their relations are given below:

$$k_F = \frac{1}{\hbar}\sqrt{2m\mathcal{E}_F}, \quad \lambda_F = \frac{2\pi}{k_F}, \quad v_F = \frac{\hbar k_F}{m}.$$

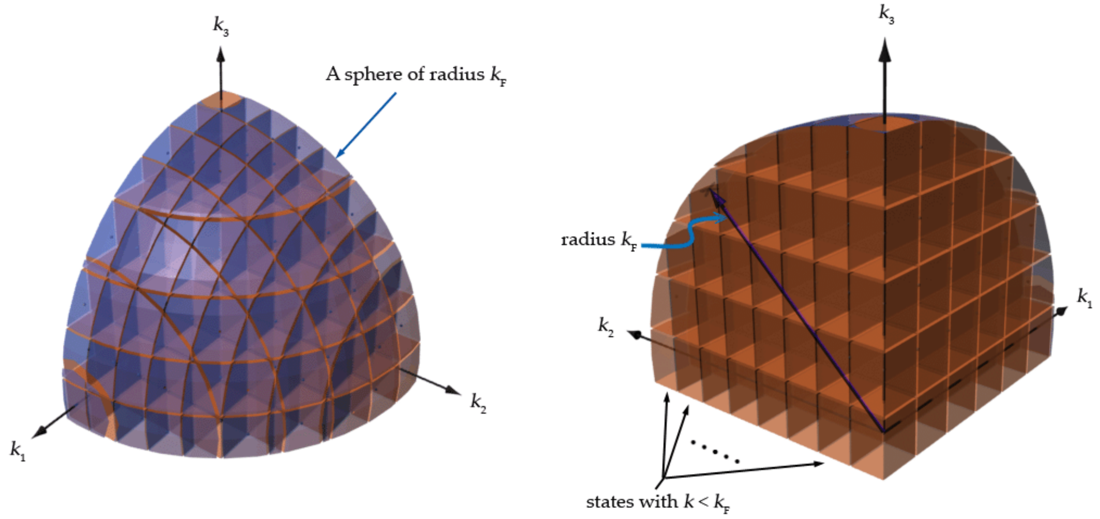

Figure 2.2: Two drawings of a Fermi sphere [4]. The occupied states have momentum $k < k_F$, creating a sphere of radius k_F in **k**-space.

We can calculate various ground state physical quantities in terms of the Fermi energy. First, we can find a relation between the electron number density $n = N/\mathcal{V}$, a macroscopic quantity, and the microscopic quantity k_F. We start with the number operator $\hat{N} = \sum_{\mathbf{k}} n_{\mathbf{k}} = \sum_{\mathbf{k}} \hat{c}^\dagger_{\mathbf{k}}\hat{c}_{\mathbf{k}}$:

$$\begin{aligned} N = \langle FS|\hat{N}|FS\rangle &= \sum_\sigma \langle FS|\sum_{\mathbf{k}} n_{\mathbf{k}}|FS\rangle \\ &= \sum_\sigma \frac{\mathcal{V}}{(2\pi)^3}\int \mathrm{d}\mathbf{k}\,\langle FS|n_{\mathbf{k}}|FS\rangle. \end{aligned} \tag{2.2.13}$$

Since electrons only have $k < k_F$ in the ground state, $n_{\mathbf{k}}|FS\rangle = |FS\rangle$ when $k < k_F$ is true and zero otherwise. We can write this as $n_{\mathbf{k}}|FS\rangle = \theta(k_F - k)|FS\rangle$ and the integration is done as follows,

$$\begin{aligned} N &= \sum_\sigma \frac{\mathcal{V}}{(2\pi)^3} \int \mathrm{d}\mathbf{k}\, \theta(k_F - k) \langle\, FS \,|\, FS \,\rangle \\ &= 2\frac{\mathcal{V}}{(2\pi)^3} \int_0^{k_F} \mathrm{d}k\, k^2 \int_{-1}^{1} \mathrm{d}\cos\theta \int_0^{2\pi} \mathrm{d}\phi \\ &= \frac{\mathcal{V}}{3\pi^2} k_F^3 \; . \end{aligned} \tag{2.2.14}$$

We obtain the very important relation:

$$k_F^3 = 3\pi^2 n. \tag{2.2.15}$$

Since n is directly measurable, we can use this to directly measure the values of the microscopic Fermi quantities.

Similarly, the ground state energy $E^{(0)}$ is expressed in terms of the Fermi energy as

$$\begin{aligned} E^{(0)} &= \langle\, FS \,|\hat{\mathcal{H}}_{jel}|\, FS \,\rangle = \sum_{\mathbf{k}\sigma} \frac{\hbar^2 k^2}{2m} \langle\, FS \,|n_{\mathbf{k}}|\, FS \,\rangle = 2\frac{\mathcal{V}}{(2\pi)^3} \frac{\hbar^2}{2m} \int \mathrm{d}\mathbf{k}\, k^2 \theta(k_F - k) \\ &= \frac{\mathcal{V}}{5\pi^2} \frac{\hbar^2}{2m} k_F^5 = \frac{3}{5} N \mathcal{E}_F. \end{aligned} \tag{2.2.16}$$

A very important quantity in solid state physics is the density of states (DOS), which takes different forms but always describes the amount of states that are available to be occupied. The DOS as a function of energy counts the number ΔN of states in the energy interval $\Delta\mathcal{E}$ around the energy $\mathcal{E}$, so that $D(\mathcal{E}) = \frac{\mathrm{d}N}{\mathrm{d}\mathcal{E}}$, and the density of states per volume is given by $d(\mathcal{E}) = D(\mathcal{E})/\mathcal{V} = \frac{\mathrm{d}n}{\mathrm{d}\mathcal{E}}$. Using (2.2.15), we find their relations for the free Fermi gas (jellium model):

$$\mathcal{E}_F = \frac{\hbar^2}{2m} k_F^2 = \frac{\hbar^2}{2m} (3\pi^2)^{\frac{2}{3}}\, n^{\frac{2}{3}} \Rightarrow n(\mathcal{E}) = \frac{1}{3\pi^2} \left(\frac{2m}{\hbar^2} \right)^{\frac{3}{2}} \mathcal{E}^{\frac{3}{2}}, \text{for } \mathcal{E} > 0, \tag{2.2.17}$$

$$d(\mathcal{E}) = \frac{\mathrm{d}n}{\mathrm{d}\mathcal{E}} = \frac{1}{2\pi^2}\left(\frac{2m}{\hbar^2}\right)^{\frac{3}{2}} \mathcal{E}^{\frac{1}{2}}\,\theta(\mathcal{E}), \quad D(\mathcal{E}) = \frac{\mathrm{d}N}{\mathrm{d}\mathcal{E}} = \frac{\mathcal{V}}{2\pi^2}\left(\frac{2m}{\hbar^2}\right)^{\frac{3}{2}} \mathcal{E}^{\frac{1}{2}}\,\theta(\mathcal{E}). \quad (2.2.18)$$

The DOS is very useful for calculating physical quantities. For instance, the particle number N can be calculated with $N = \int \mathrm{d}\mathcal{E}\, D(\mathcal{E})$, and the total energy can be calculated by $E^{(0)} = \int \mathrm{d}\mathcal{E}\, \mathcal{E} D(\mathcal{E})$.

The above calculations are done in 3 dimensions. For systems with lower dimensionalities the relations can be derived analogously [19]. In the case of materials that exhibit 2-dimensional behaviour, the expression for the DOS changes to

$$D(\mathcal{E}) = \mathcal{V}\frac{m}{\pi\hbar^2}, \quad (2.2.19)$$

which does not depend on energy.

2.3 Density functional theory

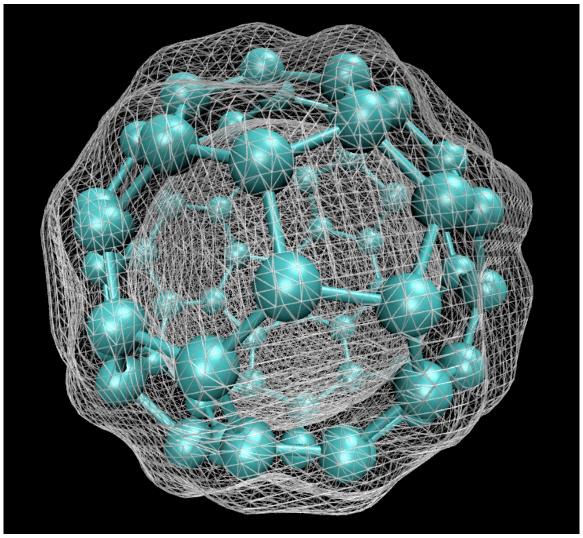

Figure 2.3: Isosurface of the ground-state density of C_{60} fullerene as calculated with DFT [5].

The jellium model is clearly too crude for real solids which are made of real atoms and where electron-electron interactions cannot be neglected. In this section, we shall discuss the density functional theory (DFT) which is a very good approximation for solving the electronic structure of most solid state systems. In DFT, the most important quantity is the electron density $n(\mathbf{r})$ which describes the probability to find any electron in a certain volume element d$\mathbf{r}$. Without spin dependence, it is defined as:

$$n(\mathbf{r}) = N \int |\Psi(\mathbf{r}, \mathbf{r}_2, \ldots, \mathbf{r}_N)|^2 \, d\mathbf{r}_2 \ldots d\mathbf{r}_N. \tag{2.3.1}$$

DFT [21, 22, 23, 24] uses the electron density as the main variable. Since the electron density only depends on three spatial variables and one spin variable, it is in principle a much simpler way for computing electronic structures as compared to solving the many-body wave function of Eq. (2.1.10). DFT has become the weapon of choice for studying condensed matter physics, materials science, biology and various disciplines of engineering. Its original discoverer, Prof. Walter Kohn, was awarded the Nobel Prize in 1998. In this chapter, we will give a brief outline of DFT, starting with a few important theorems and showing its strengths and limitations.

2.3.1 The Thomas-Fermi theory

The Thomas-Fermi (TF) theory can be considered a form of DFT [25, 26]. It uses relation (2.2.15) to approximate the electron density $n(\mathbf{r})$ in terms of the Fermi momentum $\mathbf{p}_F = \hbar \mathbf{k}_F$ and obtain an explicit form of the free Fermi gas kinetic energy functional as

$$T_{\mathrm{TF}}[n(\mathbf{r})] = C_F \int n^{5/3}(\mathbf{r}) \, \mathrm{d}^3\mathbf{r},$$

where the constant is equal to $C_F = \frac{3}{10}\hbar^2(3\pi^2)^{2/3}$. Since this included only the contribution of the free non-interacting electrons to the total kinetic energy and neglected all the nonclassical exchange and correlation effects, the TF model is wildly inaccurate for all but the simplest systems: for instance it is unable to predict molecular bonding. Despite these serious problems, it was the first attempt to put the electron density to use at a time it was not known if this usage was theoretically justified. Hohenberg and Kohn subsequently put the idea on a solid mathematical foundation, after which Kohn and Sham extended it to the modern version of density functional theory.

2.3.2 Hohenberg-Kohn theorems

The two Hohenberg-Kohn theorems [22] establish the theoretical foundation of DFT, proving that it is indeed a viable way for describing the many electron problem. They will be briefly stated in this section. For a more detailed review and derivation, we refer to [21, 24].

The first Hohenberg-Kohn theorem states that the ground state properties of an N interacting electron system are functionals depending on the ground state electron density. In other words, the ground state electron density uniquely determines the external potential $V_{ext}(\mathbf{r})$ and thus all properties of the system, including its many-body wave function. The second HK theorem states that the total energy functional obtains its minimal value at the correct ground state electron density in the external potential $V_{ext}(\mathbf{r})$. This energy is the ground state energy of the system.

The starting Hamiltonian for DFT is the one shown earlier at (2.1.9),

$$\hat{\mathcal{H}} = \hat{T} + \hat{V}_{ee} + \hat{V}_{ext}. \tag{2.3.2}$$

We introduce the universal Hohenberg-Kohn functional, defined as

$$\begin{aligned} F_{\mathrm{HK}}[n] &\equiv \langle\, \Psi \,|\hat{T} + \hat{V}_{ee}|\, \Psi \,\rangle \\ &= T[n] + V_{ee}[n]. \end{aligned} \tag{2.3.3}$$

This functional is not dependent on the specific system or the external potential, and is valid everywhere. If there existed an analytical expression for F_{HK}, then DFT would be an exact theory. The total energy functional is then given in terms of $V_{ext}(\mathbf{r})$ and

F_{HK} as

$$\begin{aligned} E[n] &= \langle\, \Psi \,|\hat{T} + \hat{V}_{ee} + \hat{V}_{ext}|\, \Psi \,\rangle \\ &= \int V_{ext}(\mathbf{r}) n(\mathbf{r})\, \mathrm{d}\mathbf{r} + F_{\mathrm{HK}}[n]. \end{aligned} \tag{2.3.4}$$

Using this, we can rewrite the second theorem as

$$E[n] \geq E_{\mathrm{GS}}, \tag{2.3.5}$$

where the equality holds if and only if $n = n_{\mathrm{GS}}$, the ground state electron density. We can extract the classical Coulomb energy from $V_{ee}[n]$ to obtain

$$V_{ee}[n] = \frac{1}{2} \int \frac{n(\mathbf{r})\, n(\mathbf{r}')}{|\mathbf{r} - \mathbf{r}'|}\, \mathrm{d}\mathbf{r}\mathrm{d}\mathbf{r}' + W_{ee}[n] \equiv V_H[n] + W_{ee}[n], \tag{2.3.6}$$

where the first term is the Hartree potential describing the classical electrostatics, and the functional $W_{ee}[n]$ will be a major part of the nonclassical exchange-correlation energy.

It should be noted again that, should the analytical forms of $T[n]$ and $W_{ee}[n]$ be known, this theory becomes an exact theory. Since they are not known, some further approximations will be required. The most widely used extension is the Kohn-Sham (KS) theory which further rewrites the functional $E[n]$ in a way to better approximate the kinetic energy functional $T[n]$, as this part is the major source of errors in DFT. KS-DFT maps the problem of many interacting electrons to one of non-interacting electrons moving in a self-consistent field, which greatly simplifies the many electron problem. Another important thing to note is that DFT is essentially a ground state theory. Extending DFT for excited states calculations is an ongoing research field [27].

2.3.3 Self-consistent Kohn-Sham equations

Kohn and Sham came up with the idea of rewriting the total energy functional of (2.3.4) with the relations (2.3.3) and (2.3.6) as

$$E[n] = T_0[n] + \frac{1}{2}\int \frac{n(\mathbf{r})\, n(\mathbf{r}')}{|\mathbf{r}-\mathbf{r}'|}\, \mathrm{d}\mathbf{r}\mathrm{d}\mathbf{r}' + \int V_{ext}(\mathbf{r})n(\mathbf{r})\, \mathrm{d}\mathbf{r} + E_{xc}[n], \tag{2.3.7}$$

where $T_0[n]$ describes the kinetic energy of a system of non-interacting electrons that has the same density $n(\mathbf{r})$ as the original system. This form, although not the true many-electron kinetic energy, is a good approximation and it justifies their choice of the expression for the total energy functional. The second and third terms are the classical Hartree term and external potential energy term. All the non-classical contributions have been put inside the fourth term, the exchange-correlation energy functional E_{xc} defined as

$$E_{xc} = W_{ee}[n] + T[n] - T_0[n]. \tag{2.3.8}$$

After applying the variational principle to (2.3.7) [23] and defining the exchange-correlation potential as a functional derivative,

$$V_{xc}(\mathbf{r}) \equiv \frac{\delta E_{xc}[n]}{\delta n(\mathbf{r})},$$

we obtain the Kohn-Sham (KS) equation:

$$\left[-\frac{1}{2}\nabla^2 + V_{eff}(\mathbf{r})\right]\phi_i = \epsilon_i \phi_i, \tag{2.3.9}$$

where the Kohn-Sham effective potential is defined as

$$V_{eff}(\mathbf{r}) = V_{ext}(\mathbf{r}) + \int \frac{n(\mathbf{r}')}{|\mathbf{r}-\mathbf{r}'|}\, \mathrm{d}\mathbf{r}' + V_{xc}(\mathbf{r}), \tag{2.3.10}$$

and the wave functions ϕ_i are related to the ground state electron density by

$$n(\mathbf{r}) = \sum_{i}^{N} |\phi_i(\mathbf{r})|^2 \quad , \tag{2.3.11}$$

where the sum is over the occupied Kohn-Sham orbitals. Equations (2.3.9 - 2.3.11) form the Kohn-Sham equations. The great advantage of the KS equations is that the wave functions ϕ_i describe a set of non-interacting electrons moving in a self-consistent effective potential field, greatly simplifying calculations compared to the original interactive many-body problem.

The form of these equations means they have to be solved self-consistently because the effective potential V_{eff} depends on the density. Usually, one starts with an initial guess of $n(\mathbf{r})$, proceeds to calculate V_{eff} by Eq.(2.3.10) and then solves ϕ_i from the KS equations, after which a new density is constructed from Eq.(2.3.11). The new density then becomes the input for the next iteration step. This process is repeated until self-consistency is achieved.

The above description only holds for spinless, non-magnetic, and non-relativistic problems. KS-DFT has been extended to include these effects without too much difficulty. To save space these further extensions will not be reviewed in this thesis.

2.3.4 Exchange-correlation functionals

Analogous to the original HK-DFT, Kohn-Sham theory would be exact if E_{xc} were known exactly. This is not the case, yet exchange and correlation effects play such a large role in determining the physical properties of the system. It is thus of great importance to determine approximate forms of this exchange-correlation functional, and development of accurate functionals is still a very active field of research.

There are many popular XC functionals available and can typically be grouped into three types: the local density approximations (LDA), the semi-local approximations

(GGA), and the non-local approximations (hybrid functionals, LDA+U). They each have strengths and deficiencies and thus have to be chosen according to the particular problem at hand.

The LDA approximates $E_{xc}[n(\mathbf{r})]$ by taking the density $n(\mathbf{r}) \approx n$ constant as in the uniform electron gas discussed in Section 2.2, and is reasonably accurate even if the actual electron gas is weakly inhomogeneous, i.e. if the density varies very slowly. The LDA has been observed to be quite successful for many different materials but it has a number of well-known deficiencies, such as overestimating the binding energy and underestimating the bond length and band gaps in semiconductors and insulators. In the present work, the LDA functional of von Barth and Hedin [28] will be used. This calculates the lattice constant of graphene to be 2.45 Å, which is in excellent agreement with the experimental value of 2.46 Å.

2.4 Summary

In this chapter, we have outlined the basic concepts of electronic structure theory of condensed matter physics. We have mentioned a few important approximations to make calculations much easier and have explained a few concepts in condensed matter theory such as the reciprocal space and the density of states. So far, we have neglected the all-important electron-electron interactions. We then reviewed density functional theory which does include part of these interactions, and is the most widely used atomistic theory in materials science fields, including solid state physics, quantum chemistry and many others. In the following chapter, we will proceed with a method of solving the Kohn-Sham equations that works very well for solid crystals: the LMTO method.

3

The LMTO method

In this Chapter, we review the linear muffin tin orbital (LMTO) method [29, 30, 31] for self-consistently solving the Kohn-Sham equation. The LMTO method, especially in its tight-binding (TB-LMTO) form [32], is a highly efficient method that is able to handle large numbers of atoms such as several thousands or even more [33, 34]. Here, the term "tight-binding" only means that long-range screening is applied; the method remains fully self-consistent. The LMTO method also allows for efficient implementation of the disorder theory which will be outlined in a later section.

3.1 Solving the Kohn-Sham equations

To solve the KS equations of (2.3.9 - 2.3.11), the one-electron wave functions need to be expanded in terms of an appropriately chosen basis set:

$$\psi_{n\mathbf{k}}(\mathbf{r}) = \sum_i c_{i,n\mathbf{k}}\, \chi_{i\mathbf{k}}(\mathbf{r}), \tag{3.1.1}$$

where the basis functions $\{\chi_{i\mathbf{k}}(\mathbf{r})\}$ form a complete set. The Hamiltonian can then be transformed into a matrix form in the Hilbert space spanned by these orbitals, and one defines the Hamiltonian and overlap matrices of H_{ij} and O_{ij} as

$$H_{ij} = \langle\, \chi_i \,|\hat{\mathcal{H}}|\, \chi_j \,\rangle \tag{3.1.2}$$

$$O_{ij} = \langle\, \chi_i \,|\, \chi_j \,\rangle. \tag{3.1.3}$$

The energy eigenvalue equation then becomes

$$\det\left[H - \mathcal{E}_n O\right] = 0. \tag{3.1.4}$$

To solve the matrix equation (3.1.4) efficiently, one has to choose a basis set that is mathematically simple and describes the particular problem accurately, while being small enough to make the solution computationally feasible. There are many different choices for $\{\chi_i\}$ available, each suited for solving different kinds of problems. The various methods of DFT structure calculations are distinguished by the choice of basis sets they make. Examples of fixed basis sets are linear combinations of atomic orbitals (LCAO), and Gaussian orbitals (LCGO). Examples of partial-wave basis sets are Augmented plane wave (APW, LAPW) and muffin tin orbitals (MTO, LMTO).

After the basis set has been chosen, we can iterate the KS equations until self-consistency is reached. This gives rise to an additional, purely mathematical problem of efficient convergence. Usually a direct iteration or even a simple mixing scheme will end up diverging, so certain specialized mixing schemes [35] are used in order to make the calculation converge reasonably fast.

3.2 Atomic sites

The LMTO method is based on the muffin-tin approximation (MT) [29], which puts muffin-tin spheres at the atomic sites. Inside these spheres the potential is taken to be spherically symmetric. In the so-called interstitial region between the spheres, the potential is approximated as being flat. The wave functions are thus separated into two parts. Inside the spheres, the wave functions can be expanded in terms of spherical harmonics and the eigenvalues of the radial Schrödinger equation. The interstitial part can be represented in terms of plane waves. At the sphere boundaries, these two parts are connected in a smooth, continuous way. This allows for rapidly varying functions close to atomic sites while efficiently representing them as plane waves when the distance to the atoms is relatively large, making this approximation a very reasonable one for studying solids. The MT approximation is also used in other methods, such as LAPW and the Korringa-Kohn-Rostocker Green's function method (KKR) which is very similar to the LMTO method.

The MT potential $V(\mathbf{r}) = V_{MT}(r_{\mathbf{R}})$ is defined as

$$V_{MT}(r_{\mathbf{R}}) = V_{\mathbf{R}}(r_{\mathbf{R}}), \qquad r_{\mathbf{R}} \leq s_{\mathbf{R}}, \tag{3.2.1a}$$

$$V_{MT}(r_{\mathbf{R}}) = V_{\mathrm{MTZ}}, \qquad r_{\mathbf{R}} \geq s_{\mathbf{R}}, \tag{3.2.1b}$$

where $\mathbf{r_R} = \mathbf{r} - \mathbf{R}$ is the distance to the center, $s_{\mathbf{R}}$ the radius, and $V_{\mathbf{R}}(r_{\mathbf{R}})$ the spherically symmetric potential inside the $\mathbf{R}$-th MT sphere. The atomic sphere approximation (ASA), which is an important part of the present work, takes $V_{\mathrm{MTZ}} = E$. We will review the ASA later on in this section.

The Schrödinger equation is then given as

$$\left[-\nabla^2 + \sum_{\mathbf{R}} V_{MT}(r_R) - E\right]\Psi = 0, \tag{3.2.2}$$

where the sum extends over the whole crystal. As noted before, construction of the LMTO basis functions $\chi_{\mathbf{R}L}$, where L is the combined angular momentum index $L = (l, m)$, requires choosing the functions $\varphi_{\mathbf{R}L}(\mathbf{r}, E)$ inside the $\mathbf{R}$-th sphere (head) and outside of it (tail), and a reasonably complete envelope function in the interstitial region. Then, after choosing reasonable expressions for these functions, we can glue them together to form the LMTO basis set for the entire space.

The Schrödinger equation inside the MT sphere is:

$$\left[-\nabla^2 + \sum_{\mathbf{R}} V_{\mathbf{R}}(r) - E\right]\varphi_{\mathbf{R}L}(\mathbf{r}, E) = 0. \tag{3.2.3}$$

We can write down the solution for $\varphi_{\mathbf{R}L}(\mathbf{r},E)$ in a general form as

$$\varphi_{\mathbf{R}L}(\mathbf{r},E)=\varphi_{\mathbf{R}l}(r,E)\,Y_L(\hat{\mathbf{r}}),\tag{3.2.4}$$

where $Y_L(\hat{\mathbf{r}})$ are spherical harmonics. The radial part is obtained by solving the radial Schrödinger equation,

$$\left[-\frac{\partial^2}{\partial r^2}-\frac{2}{r}\frac{\partial}{\partial r}+\frac{l(l+1)}{r^2}+V_{\mathbf{R}}(r)-E\right]\varphi_{\mathbf{R}l}(r,E)=0.\tag{3.2.5}$$

Normalizing the radial part within the MT spheres gives us the normalization relation

$$\int_0^{s_{\mathbf{R}}}\varphi^2_{\mathbf{R}l}(r,E)\,r^2\,\mathrm{d}r=1,\tag{3.2.6}$$

and, taking its energy derivative, we obtain an orthogonality relation which is given by

$$\int_0^{s_{\mathbf{R}}}\varphi_{\mathbf{R}l}(r,E)\,\dot{\varphi}_{\mathbf{R}l}(r,E)\,r^2\,\mathrm{d}r=0,\tag{3.2.7}$$

where $\dot{\varphi}_{\mathbf{R}l}$ is defined as the energy derivative $\frac{\partial}{\partial E}\varphi_{\mathbf{R}l}$. $\varphi_{\mathbf{R}l}$ and $\dot{\varphi}_{\mathbf{R}l}$ are both truncated inside the $\mathbf{R}$-th sphere of radius $s_{\mathbf{R}}$ and will be used to construct the basic head and tail functions. They are both orthogonal to the core electron states, so the constructed basis set will also be orthogonal to the core electron orbitals.

3.3 *The envelope function*

In the interstitial region where there is no atomic sphere and the potential is flat, the Schrödinger equation turns into

$$\left[-\nabla^2-\kappa^2\right]\chi_{\mathbf{R}L}(\mathbf{r},\kappa)=0,\tag{3.3.1}$$

where $\chi_{\mathbf{R}L}(\mathbf{r},\kappa)$ is the envelope function and $\kappa^2=E-V_{\mathrm{MTZ}}$ is the electron kinetic energy in the interstitial region. The ASA takes this kinetic energy to be 0, so that

(3.3.1) reduces to Laplace's equation,

$$\nabla^2 \chi_{\mathbf{R}L}(\mathbf{r}) = 0. \tag{3.3.2}$$

First, let's consider the system where there are no atomic spheres so that Eq. (3.3.2) will be valid everywhere. As before, the general solution is

$$\chi_L(\mathbf{r}) = \chi_l(r)\, Y_L(\hat{\mathbf{r}}), \tag{3.3.3}$$

with the radial equation now being

$$\left[-\frac{\partial^2}{\partial r^2} - \frac{2}{r}\frac{\partial}{\partial r} + \frac{l(l+1)}{r^2} \right] \chi_l(r) = 0. \tag{3.3.4}$$

There are two independent solutions to Laplace's equation. According to the asymptotic behaviour for $r_{\mathbf{R}} \to \infty$, the regular solutions are given by (changing back to $\mathbf{r_R}$)

$$J^0_{\mathbf{R}L}(\mathbf{r_R}) = \frac{1}{2(2l+1)} \left(\frac{r_{\mathbf{R}}}{w} \right)^l Y_L(\hat{\mathbf{r}}), \tag{3.3.5}$$

and the irregular solutions by

$$K^0_{\mathbf{R}L}(\mathbf{r_R}) = \left(\frac{r_{\mathbf{R}}}{w} \right)^{-l-1} Y_L(\hat{\mathbf{r}}), \tag{3.3.6}$$

where w is introduced to make the solutions dimensionless. The two solutions $K^0_{\mathbf{R}L}$ at site $\mathbf{R}$ and $J^0_{\mathbf{R}'L'}$ at a different site $\mathbf{R}'$, ($\mathbf{R}' \neq \mathbf{R}$) are related to each other by the following expression:

$$K^0_{\mathbf{R}L}(\mathbf{r_R}) = -\sum_{L'} J^0_{\mathbf{R}'L'}(\mathbf{r_{R'}})\, S^0_{\mathbf{R}L,\mathbf{R}'L'}, \tag{3.3.7}$$

where $S^0_{\mathbf{R}L,\mathbf{R}'L'}$ are called canonical structure constants, independent of the crystal potential, and given in the explicit form as

$$S^0_{\mathbf{R}L,\mathbf{R}'L'} = \sum_{L''} (-1)^{l'+1} \frac{8\pi(2l''-1)!!\, C_{LL'L''}}{(2l-1)!!\,(2l'-1)!!} K^0_{L''}(\mathbf{R}'-\mathbf{R}), \tag{3.3.8}$$

where $C_{LL'L''}$ are the Gaunt coefficients given by

$$C_{LL'L''} = \int Y_L(\hat{\mathbf{r}})\, Y_{L'}(\hat{\mathbf{r}})\, Y_{L''}(\hat{\mathbf{r}})\, \mathrm{d}^2\hat{\mathbf{r}}.$$

The structure constant matrix S^0 is real, symmetric, and has an inverse power law dependence on the distance $|\mathbf{R}-\mathbf{R}'|$:

$$S^0_{\mathbf{R}L,\mathbf{R}'L'} \propto \left(\frac{w}{|\mathbf{R}-\mathbf{R}'|}\right)^{l+l'+1}. \tag{3.3.9}$$

Since $K^0_{\mathbf{R}L}$ is a long-range function that decays slowly as an inverse power law of $\mathbf{r}_\mathbf{R}$, a screening procedure is introduced to localize this function for reasons of efficient computation. We introduce the screening procedure in the next section.

3.4 Long range screening and the tight binding MTO

We will briefly go over the screening procedure to obtain a localized envelope function. For further details, Ref. [32] can be consulted. To start, we separate the space into different regions and separate the functions accordingly. We define $|\ \rangle$ for functions that are truncated inside the Wigner-Seitz (WS) cell centered around $\mathbf{R}$, and $|\ \rangle^\infty$ for functions extending over all space. We then rewrite the bare envelope function in terms of its regional contributions,

$$|\, K^0_{\mathbf{R}L}\, \rangle^\infty = |\, K^0_{\mathbf{R}L}\, \rangle - \sum_{\mathbf{R}'} \sum_{L'} |\, J^0_{\mathbf{R}'L'}\, \rangle S^0_{\mathbf{R}'L',\mathbf{R},L}, \tag{3.4.1}$$

where the contributions inside other WS cells of $\mathbf{R}' \neq \mathbf{R}$ are expanded using relation (3.3.7). The sum over $\mathbf{R}$ goes over all atomic sites, making the resulting function

$|\, K^0_{\mathbf{R}L}\, \rangle^\infty$ extend over all space. In compact notation with the sums being implied, Eq. (3.4.1) can also be written as

$$|\, K^0\, \rangle^\infty = |\, K^0\, \rangle - |\, J^0\, \rangle S^0. \tag{3.4.2}$$

Adding a screening part $\alpha_{\mathbf{R}l}$ to the regular solution $|\, J^0\, \rangle$, we obtain the following function,

$$|\, J^\alpha\, \rangle \equiv |\, J^0\, \rangle - \alpha_{\mathbf{R}l} |\, K^0\, \rangle. \tag{3.4.3}$$

We can then express the screened envelope function in the entire space as

$$|\, K^\alpha\, \rangle^\infty = |\, K^0\, \rangle - |\, J^\alpha\, \rangle S^\alpha, \tag{3.4.4}$$

where the screened structure constants are defined as

$$S^\alpha = S^0 \left(1 - \alpha S^0\right)^{-1}. \tag{3.4.5}$$

We can also express this α-screened function in terms of the bare envelope function $|\, K^0\, \rangle^\infty$, obtaining

$$|\, K^\alpha\, \rangle^\infty = |\, K^0\, \rangle^\infty (1 + \alpha S^\alpha). \tag{3.4.6}$$

Using this screening, an exponential decay over the distance can be obtained for $|\, K^\alpha\, \rangle^\infty$. The rate of decay can be adjusted by modifying $\alpha_{\mathbf{R}l}$ per orbital, and one can choose them such that $S^\alpha_{\mathbf{R}'L',\mathbf{R},L}$ decay very fast, making them range over only the first- and second-nearest neighbour sites. This greatly reduces the computational effort while still being a reasonable approximation. This method is usually called tight-binding MTO (TB-MTO).

3.5 Wave function matching

Now that we have solutions for both inside and outside the MT spheres, we have to match (augment) them together to get the full TB-MTO basis set $|\,\chi^{\alpha}_{\mathbf{R}L}\,\rangle^{\infty}$. To do this, we divide the regions in a different way using MT spheres instead of WS cells, and redefine $|\,\rangle$ to stand for truncation within the MT sphere. We then rewrite Eq. (3.4.4) as

$$|\,K^{\alpha}\,\rangle^{\infty} = |\,K^{0}\,\rangle - |\,J^{\alpha}\,\rangle S^{\alpha} + |\,K^{\alpha}\,\rangle^{i}, \tag{3.5.1}$$

where $|\,K^{\alpha}\,\rangle^{i}$ is the wave function in the interstitial region given by

$$|\,K^{\alpha}\,\rangle^{i} = |\,K^{\alpha}\,\rangle^{\infty} - \big(|\,K^{0}\,\rangle - |\,J^{\alpha}\,\rangle\big)\,. \tag{3.5.2}$$

We can now augment the wave function inside the MT spheres and leave the envelope function in the interstitial region unchanged. The full solution must equal to the regular solution of (3.4.4) inside the spheres and the decaying solution of the Laplace equation outside of the spheres, while the condition of smoothness means that the functions and their first derivatives must be made equal at the sphere boundary.

We first augment the wave function $|\,J^{\alpha}_{\mathbf{R}L}\,\rangle \to |\,\tilde{J}^{\alpha}_{\mathbf{R}L}\,\rangle$ to a regular function whose form will become clear in the next section. The requirements of continuity are as follows:

$$\begin{aligned} \tilde{J}^{\alpha}_{\mathbf{R}L}(s_R) &= J^{\alpha}_{\mathbf{R}L}(s_R), \\ \frac{\partial}{\partial r}\tilde{J}^{\alpha}_{\mathbf{R}l}(r)\bigg|_{s_R} &= \frac{\partial}{\partial r}J^{\alpha}_{\mathbf{R}l}(r)\bigg|_{s_R}\,. \end{aligned}$$

A useful technique to match functions smoothly at $r = s_R$, with the term smooth standing for continuity and differentiability at the aforementioned location, is to use the Wronskian of two functions defined by:

$$W\left\{f_1(r), f_2(r)\right\}_{r=s_R} = r^2\left[f_1(r)f_2'(r) - f_1'(r)f_2(r)\right]_{r=s_R}. \tag{3.5.3}$$

Additionally, we define the so-called potential function $P^{\alpha}_{\mathbf{R}l}(E)$ and normalization function $N^{\alpha}_{\mathbf{R}l}(E)$ as:

$$P^{\alpha}_{\mathbf{R}l}(E) = \frac{W\{K^0, \varphi(E)\}_{\mathbf{R}l}}{W\{\tilde{J}^{\alpha}, \varphi(E)\}_{\mathbf{R}l}} = \frac{W\{K^0, \varphi(E)\}_{\mathbf{R}l}}{W\{J^{\alpha}, \varphi(E)\}_{\mathbf{R}l}} \tag{3.5.4}$$

and

$$N^{\alpha}_{\mathbf{R}l}(E) = \frac{W\{\tilde{J}^{\alpha}, K^0\}_{\mathbf{R}l}}{W\{\tilde{J}^{\alpha}, \varphi(E)\}_{\mathbf{R}l}} = \frac{W\{J^{\alpha}, K^0\}_{\mathbf{R}l}}{W\{J^{\alpha}, \varphi(E)\}_{\mathbf{R}l}} = \left[\frac{w}{2}\dot{P}^{\alpha}_{\mathbf{R}l}(E)\right]^{\frac{1}{2}}. \tag{3.5.5}$$

Using these definitions, we can write $|\, K^0_{\mathbf{R}L}\,\rangle$ as

$$K^0_{\mathbf{R}L}(r) \longrightarrow N^{\alpha}_{\mathbf{R}l}(E)\,\varphi_{\mathbf{R}l}(r,E) + P^{\alpha}_{\mathbf{R}l}(E)\,\tilde{J}^{\alpha}_{\mathbf{R}L}. \tag{3.5.6}$$

Now we can write down a basis set for the energy-dependent MTO over the whole space as

$$|\,\chi^{\alpha}(E)\,\rangle^{\infty} = N^{\alpha}(E)\,|\,\varphi(E)\,\rangle + (P^{\alpha}(E) - S^{\alpha})\,|\,\hat{J}^{\alpha}\,\rangle + |\,K^{\alpha}\,\rangle^{i}, \tag{3.5.7}$$

where, again, $|\;\rangle^{\infty}$ is defined as extending over all space, $|\;\rangle$ stands for functions truncated inside the MT spheres, and $|\;\rangle^{i}$ are functions truncated inside the interstitial region. It is important to note that this basis is energy dependent.

3.6 Energy linearization

Since it is very hard to work with a basis set that is energy dependent, we will define $\tilde{J}^{\alpha}$ in equation (3.5.7) such that the energy dependence of $|\,\chi^{\alpha}(E)\,\rangle^{\infty}$ vanishes to first order when expanding around $E = \mathcal{E}_{\nu}$, where the energy $\mathcal{E}_{\nu}$ is chosen appropriately for the problem. Such a linearized MTO basis is denoted as LMTO.

Setting $|\,\dot{\chi}^\alpha(E)\,\rangle^\infty = 0$ at $E = \mathcal{E}_\nu$ and evaluating (3.5.7) we get

$$|\,\dot{\chi}^\alpha(E)\,\rangle^\infty|_{\mathcal{E}_\nu} = N^\alpha\,|\,\dot{\varphi}^\alpha\,\rangle + \dot{P}^\alpha\,|\,\tilde{J}^\alpha\,\rangle = 0, \tag{3.6.1}$$

where

$$|\,\dot{\varphi}^\alpha\,\rangle = |\,\varphi\,\rangle o^\alpha + |\,\dot{\varphi}\,\rangle \tag{3.6.2}$$

and o^α is defined as

$$o^\alpha = \frac{\dot{N}^\alpha}{N^\alpha} = \langle\,\varphi\,|\,\dot{\varphi}^\alpha\,\rangle. \tag{3.6.3}$$

We thus get an expression for $\tilde{J}^\alpha$,

$$|\,\tilde{J}^\alpha\,\rangle = -\frac{N^\alpha}{\dot{P}^\alpha}\,|\,\dot{\varphi}^\alpha\,\rangle = -\left(\frac{w}{2}/N^\alpha\right)\,|\,\dot{\varphi}^\alpha\,\rangle. \tag{3.6.4}$$

We can see that both $|\,\varphi\,\rangle$ and $|\,\dot{\varphi}^\alpha\,\rangle$ are components of the TB-LMTO basis function.

Expanding $|\,\chi^\alpha(E)\,\rangle^\infty$ around $E = \mathcal{E}_\nu$ with $|\,\dot{\chi}^\alpha(E)\,\rangle^\infty|_{\mathcal{E}_\nu} = 0$ gives

$$|\,\chi^\alpha(E)\,\rangle^\infty = |\,\chi^\alpha\,\rangle^\infty + (E - \mathcal{E}_\nu)^2\,|\,\ddot{\chi}^\alpha\,\rangle^\infty + \ldots \quad \approx |\,\chi^\alpha\,\rangle^\infty, \tag{3.6.5}$$

where $|\,\chi^\alpha\,\rangle^\infty = |\,\chi^\alpha(\mathcal{E}_\nu)\,\rangle^\infty$ and neglecting the higher order terms in $(E - \mathcal{E}_\nu)$. With $|\,\chi^\alpha\,\rangle^\infty$, we have thus reached the energy-independent version of MTO: LMTO. In normalized form, this is given as

$$|\,\chi^\alpha\,\rangle^\infty = \frac{1}{N^\alpha}\,|\,\chi^\alpha(\mathcal{E}_\nu)\,\rangle^\infty = (1 + o^\alpha h^\alpha)\,|\,\varphi\,\rangle + h^\alpha\,|\,\dot{\varphi}\,\rangle + \frac{1}{N^\alpha}\,|\,K^\alpha\,\rangle^i, \tag{3.6.6}$$

where h^α is a matrix defined as

$$h^\alpha = -\frac{w}{2}\frac{1}{N^\alpha}\,[P^\alpha - S^\alpha]\,\frac{1}{N^\alpha}. \tag{3.6.7}$$

In practical applications of LMTO, the energy center $\mathcal{E}_\nu$ must be chosen according to the particular problem being studied. For instance we may set $\mathcal{E}_\nu = E_F$ to obtain an accurate Fermi surface and Fermi velocity; on the other hand, for calculating an accurate charge density to investigate ground state properties, one may set $\mathcal{E}_\nu$ at the center of the occupied part of the valence band.

3.7 The atomic sphere approximation

The atomic sphere approximation (ASA) [29, 31] sets the MT spheres to be overlapping and space filling and the kinetic energy in the interstitial region to be equal to zero, so that the envelope function in the interstitial region in (3.6.6) disappears. In other words, during the calculation, we only solve the Schrödinger equation inside the spheres. For systems that are close-packed (such as metals), the ASA is a reasonable approximation. For systems that are not close-packed (such as semiconductors), we can improve the ASA by adding empty spheres with no charge to fill the open void [36]. We can see that the requirement of the spheres to fill out the space makes them overlap each other slightly. This is part of the approximation that the ASA does.

Dropping out the envelope function in the interstitial region of (3.6.6), the basis set of ASA becomes

$$|\,\chi^\alpha\,\rangle^\infty_{\mathrm{ASA}} = (1 + o^\alpha h^\alpha)\,|\,\varphi\,\rangle + h^\alpha\,|\,\dot{\varphi}\,\rangle. \tag{3.7.1}$$

Using the previously established relations of normalization Eq. (3.2.6) and orthogonality Eq. (3.2.7) of the partial waves, it is easy to write down the overlap matrix as

$$\begin{aligned} O^\infty_{\mathrm{ASA}} = {}^\infty_{\mathrm{ASA}}\langle\,\chi^\alpha\,|\,\chi^\alpha\,\rangle^\infty_{\mathrm{ASA}} &= (1 + h^\alpha o^\alpha)\,(1 + o^\alpha h^\alpha) + h^\alpha p h^\alpha \\ &\approx (1 + h^\alpha o^\alpha)\,(1 + o^\alpha h^\alpha), \end{aligned} \tag{3.7.2}$$

where

$$p = \langle\,\dot{\varphi}\,|\,\dot{\varphi}\,\rangle \tag{3.7.3}$$

is a small quantity and can be neglected in most applications. Similarly, we can get an expression for the Hamiltonian matrix:

$$\begin{aligned} H^{\infty}_{\text{ASA}} &= {}^{\infty}_{\text{ASA}}\langle\, \chi^{\alpha} \,|-\nabla^2 + V_{\mathbf{R}}(r)|\, \chi^{\alpha}\,\rangle^{\infty}_{\text{ASA}} \\ &= (1+h^{\alpha}o^{\alpha})\, h^{\alpha} + (1+h^{\alpha}o^{\alpha})\, \mathcal{E}_{\nu}\, (1+o^{\alpha}h^{\alpha}) + h^{\alpha}\mathcal{E}_{\nu} p h^{\alpha} \\ &\approx (1+h^{\alpha}o^{\alpha})\, h^{\alpha} + (1+h^{\alpha}o^{\alpha})\, \mathcal{E}_{\nu}\, (1+o^{\alpha}h^{\alpha}). \end{aligned} \tag{3.7.4}$$

With the above equations, we have obtained an expression for the Hamiltonian and overlap matrices in the TB-LMTO-ASA representation.

Neglecting the integral over the interstitial region is the major source of error of ASA and this error can be very large if used improperly. After implementation of the non-equilibrium Green's function (NEGF) based DFT formalism (NEGF-DFT, see Chapter 4), it might be impossible to correct for this error. This error can however be mitigated by making sure that the interstitial volume or the overlap volume between spheres is minimized for the atomic structure being studied. Thus, it is very important to optimize the radii of the atomic spheres to be able to obtain accurate results when ASA is applied.

3.8 *Orthogonal basis set*

By using the previous approximation (3.7.3) that $p = \langle\, \dot{\varphi} \,|\, \dot{\varphi}\,\rangle$ is small and can be neglected, we can transform the basis set of Eq. (3.7.1) into an orthogonal one by setting

$$|\, \chi^{\text{orth}}\,\rangle^{\infty}_{\text{ASA}} = (1+o^{\alpha}h^{\alpha})^{-1}\, |\, \chi^{\alpha}\,\rangle^{\infty}_{\text{ASA}} = |\, \varphi\,\rangle + h^{\alpha}(1+o^{\alpha}h^{\alpha})^{-1}\, |\, \dot{\varphi}\,\rangle. \tag{3.8.1}$$

Then, the overlap matrix turns into

$$O^{\text{orth}}_{\text{ASA}} = {}^{\infty}_{\text{ASA}}\langle\, \chi^{\text{orth}} \,|\, \chi^{\text{orth}}\,\rangle^{\infty}_{\text{ASA}} \doteq 1, \tag{3.8.2}$$

and the Hamiltonian can be written as

$$H_{\mathrm{ASA}}^{\mathrm{orth}} = {}^{\infty}_{\mathrm{ASA}}\langle\, \chi^{\mathrm{orth}} \,| - \nabla^2 + V_{\mathbf{R}}(r)|\, \chi^{\mathrm{orth}}\, \rangle^{\infty}_{\mathrm{ASA}} \doteq \mathcal{E}_{\nu} + h^{\alpha}(1 + o^{\alpha} h^{\alpha})^{-1}. \tag{3.8.3}$$

3.9 Potential parameters

The above Hamiltonian Eq. (3.8.3) can be simplified by introducing the following "potential parameters":

$$C_{\mathbf{R}l} = \mathcal{E}_{\nu} - \frac{W\{K, \varphi\}_{\mathbf{R}l}}{W\{K, \dot{\varphi}\}_{\mathbf{R}l}}, \tag{3.9.1}$$

$$\Delta_{\mathbf{R}l} = \frac{w}{2} \frac{1}{W\{K, \dot{\varphi}\}^2_{\mathbf{R}l}}, \tag{3.9.2}$$

$$\gamma_{\mathbf{R}l} = \frac{W\{J, \dot{\varphi}\}_{\mathbf{R}l}}{W\{K, \dot{\varphi}\}_{\mathbf{R}l}}. \tag{3.9.3}$$

These parameters are independent of the screening constant α and they stand for, respectively, the center ($C_{\mathbf{R}L}$), width ($\Delta_{\mathbf{R}L}$) and distortion ($\gamma_{\mathbf{R}l}$) of the $\mathbf{R}l$-th band. With this, we can rewrite the Hamiltonian matrix as

$$H_{\mathrm{ASA}}^{\mathrm{orth}} = C + \sqrt{\Delta} S (1 - \gamma S)^{-1} \sqrt{\Delta}, \tag{3.9.4}$$

where C, Δ, and γ are diagonal matrices corresponding to their respective potential parameters. We can see that $H_{\mathrm{ASA}}^{\mathrm{orth}}$ is also independent of the screening constant α.

We have now reached the point where we have an expression for the orthogonal TB-LMTO-ASA basis set and the corresponding Hamiltonian matrix with help of a few auxiliary potential parameters. We can thus use the LMTO method to solve the KS equation self-consistently and obtain the electronic structure for a wide range of electronic structure problems in solid state physics.

3.10 Summary

In this Chapter, we have briefly reviewed the TB-LMTO-ASA method as a self-consistent solution of the Kohn-Sham equations, one that is particularly well suited for describing crystals with symmetries. There are only a few potential parameters needed to describe the entire TB-LMTO basis set (P, C, Δ, γ, $|\,\varphi\,\rangle$, and $|\,\dot{\varphi}\,\rangle$), all of which are physically very well defined. This makes calculations very fast and efficient. The major challenge of this method is the necessary use of ASA which forces one to deal with atomic spheres that have to be meticulously constructed in order to obtain accurate results.

For a more formal treatise on LMTO, we refer to works reported in Refs. [29, 30, 31].

4

Quantum transport and NEGF

In this chapter, we briefly review how to calculate quantum transport properties such as the conductance and electric current from Green's functions of the open device system using atomic first principles. In particular, we will discuss the method of carrying out self-consistent DFT analysis within the Keldysh non-equilibrium Green's function formalism (NEGF) [37, 38], as well as the method for treating atomic disorder scattering.

4.1 Quantum transport

Fig. 4.1 is a plot of a two-probe device structure consisting of a scattering region sandwiched between two leads.

The leads are extended to electron reservoirs located at $z = \pm\infty$ to the left (l) and right (r) whose electrochemical potentials are μ_l and μ_r, respectively. When $\mu_l \neq \mu_r$ due to an applied bias voltage $eV = \mu_l - \mu_r$, an electric current flows through the device scattering region which will then be in a nonequilibrium state.

The two-probe system of Fig. 4.1 is naturally divided into three regions: the left/right leads and the central scattering region. Hence the Hamiltonian of such an open structure includes terms describing the leads, the central scattering region,

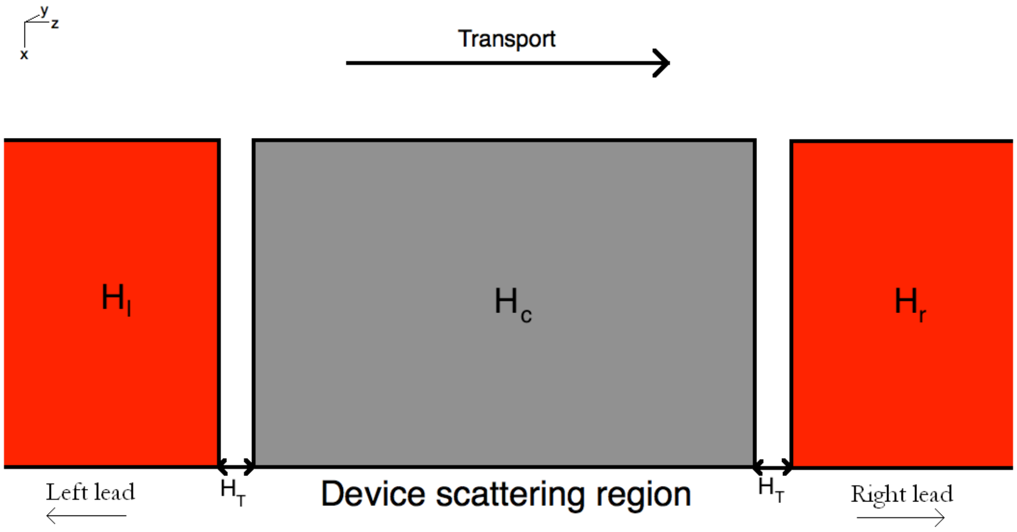

Figure 4.1: A sketch of a two-probe device. The device of the center region is connected to two semi-infinite leads. $H_{l/r}, H_c$ are the Hamiltonians describing the leads and center region, and H_T describe the interactions between the device and the leads. The transport direction is from one lead to another, through the device. The left and right leads are each assumed to be at equilibrium with electrochemical potentials μ_l and μ_r respectively. There is a voltage bias when $\mu_l \neq \mu_r$.

and the interactions between leads and the central region:

$$\hat{\mathcal{H}} = \hat{H}_{\text{leads}} + \hat{H}_{\text{center}} + \hat{H}_T \ . \tag{4.1.1}$$

$\hat{H}_{\text{leads}}$ describes the leads as

$$\hat{H}_{\text{leads}} = \sum_{\mathbf{k},l/r} \mathcal{E}_{\mathbf{k},l/r} \hat{c}^\dagger_{\mathbf{k},l/r} \hat{c}_{\mathbf{k},l/r}, \tag{4.1.2}$$

where $\hat{c}^\dagger_{\mathbf{k},l/r}$ is the creation operator for an electron in the left or right lead (l/r) and $\mathcal{E}_{\mathbf{k},l/r} = \mathcal{E}^{(0)}_{\mathbf{k},l/r} + qv_{l/r}$, with $\mathcal{E}^{(0)}_{\mathbf{k},l/r}$ the energy levels in lead l/r and $v_{l/r}$ the external voltage. $\hat{H}_{\text{center}}$ is the Hamiltonian describing the central region:

$$\hat{H}_{\text{center}} = \sum_n \left(\mathcal{E}_n + qU_n\right) \hat{d}^\dagger_n \hat{d}_n, \tag{4.1.3}$$

where $\hat{d}^\dagger_n$ creates an electron in the central region and U_n is the self-consistent Coulomb potential of the central region given by:

$$U_n = \sum_m V_{nm} \langle \hat{d}_m^\dagger \hat{d}_m \rangle, \tag{4.1.4}$$

where V_{nm} is the matrix element of the Hartree and exchange-correlation potentials as defined in Eq. (2.3.10). The last term $\hat{H}_T$ describes the interactions between the central region and the leads:

$$\hat{H}_T = \sum_{\mathbf{k}n,l/r} \left[t_{\mathbf{k}n,l/r} \hat{c}_{\mathbf{k},l/r}^\dagger \hat{d}_n + t_{\mathbf{k}n,l/r}^* \hat{d}_n^\dagger \hat{c}_{\mathbf{k},l/r} \right], \tag{4.1.5}$$

where $t_{\mathbf{k}l/rn}$ is the coupling constant between the center and the lead l/r.

Without going into the complicated derivations of the nonequilibrium Green's function (NEGF) formalism that have been well documented in literature [37, 39, 40], we will simply list the quantities that are important for this work. The retarded and advanced Green's functions of the device scattering region are given by:

$$G^{R,A}(E) = \frac{1}{E - H_0 - \Sigma_l^{R,A}(E) - \Sigma_r^{R,A}(E) \pm i0}, \tag{4.1.6}$$

where H_0 is the H_{center} of Eq. (4.1.1); $\Sigma_{l/r}^{R,A}$ are the retarded (advanced) self-energies of the left and right leads and account for the effect of the leads on the scattering region [38]. Since H_0 is the Hamiltonian for just the central region, it is a finite matrix and the Green's functions $G^{R,A}(E)$ can be calculated by direct matrix inversion. A line-width function can be defined from the self-energies:

$$\Gamma_{l/r}(E - qv_{l/r}) \equiv i \left(\Sigma_{l/r}^R(E) - \Sigma_{l/r}^A(E) \right), \tag{4.1.7}$$

which describes the coupling strength of the leads to the scattering region.

The distribution function NEGF $G^<(E)$ can be calculated by the Keldysh equation

[40] from $G^{R,A}(E)$,

$$G^{<}(E) = G^{R}(E)\,\Sigma^{<}(E)\,G^{A}(E), \tag{4.1.8}$$

where

$$\Sigma^{<}_{l/r} = i\Gamma_{l/r}(E - qv_{l/r})\,f_{l/r}(E) \tag{4.1.9}$$

is the lesser self-energy and $f_{l/r}(E)$ are the Fermi-Dirac functions of the left/right electron reservoirs. Importantly, in order to write down Eq. (4.1.9), we have assumed that the left and right leads outside of the scattering region (see Fig. 4.1) are at equilibrium and have the same chemical potentials μ_l and μ_r as that of their respective reservoirs. This is a very good assumption since device leads are usually made of good quality metal and thus have potentials equal to that of the reservoir connected to the leads at $z = \pm\infty$. Importantly, at non-equilibrium $G^{<}$ gives the electronic density matrix (thus density):

$$n(\mathbf{r}) = -\frac{i}{2\pi}\int_{-\infty}^{\infty} G^{<}(E)\ . \tag{4.1.10}$$

The advantage of NEGF lies in the fact that Eq.(4.1.10) incorporates non-equilibrium quantum statistics of the device scattering region. Of course, when there is no bias voltage ($eV = 0$), Eq. (4.1.10) reduces precisely to the equilibrium density matrix given by the retarded Green's function G^{R}, and this equilibrium density matrix corresponds exactly to what is used in the DFT discussed in the last two chapters. The formal relations between the Green's function formalism and wavefunction-based formalism (Section 2.3) can be found in Ref. [41].

Once the Green's functions are obtained, we apply the Landauer-Büttiker formalism [39, 42] to calculate quantum transport properties of the two-probe device structures (see Fig. 4.1). In particular, the transmission coefficient $T(E,V)$ and current $I(V)$ are given by:

$$T(E,V) = \mathrm{Tr}\left[\Gamma_l(E - qv_l)\,G^{R}(E)\,\Gamma_r(E - qv_r)\,G^{A}(E)\right], \tag{4.1.11}$$

$$I(V) = \frac{e^2}{h}\int \mathrm{d}E\,(f_l - f_r)\,T(E,V)\ . \tag{4.1.12}$$

Here $v_{l,r}$ are the bias voltages applied on the left and right leads, and $V = v_l - v_r$ is the bias across the central scattering region of the device (see Fig. 4.1). The equilibrium conductance of the device is obtained at zero bias $V = 0$ and the Fermi level,

$$G = \frac{2e^2}{h} T(E_f) \tag{4.1.13}$$

where e is the electron charge and h is Planck's constant.

4.2 Implementation of NEGF-DFT

The DFT discussed in Section 2.3 and Chapter 3 can describe periodic systems (such as crystals) or finite systems (such as a molecule) under equilibrium. An electronic device or transport junction such as that in Fig. 4.1 is neither periodic nor finite. It is a open system which may not be in equilibrium. To deal with those device structures, NEGF-based DFT methods (NEGF-DFT) have been developed in the past decades [38], and in this section we shall outline our method of NEGF-DFT, where the DFT method is based on TB-LMTO-ASA discussed in Chapter 3.

In TB-LMTO-ASA, the Hamiltonian in orthogonal form is given by Eq. (3.9.4). The corresponding Green's function matrix satisfies the following relation:

$$G(z) = \left[z - H^{\mathrm{orth}}\right]^{-1} = \lambda^{\alpha}(z) + \mu^{\alpha}(z)\left[P^{\alpha}(z) - S^{\alpha}\right]^{-1}\mu^{\alpha}(z), \tag{4.2.1}$$

where the diagonal matrices $P^{\alpha}(z)$, $\lambda^{\alpha}(z)$, and $\mu^{\alpha}(z)$ have elements given by

$$P^{\alpha}_{\mathbf{R}l}(z) = \frac{z - C_{\mathbf{R}l}}{\Delta_{\mathbf{R}l} + (\gamma_{\mathbf{R}l} - \alpha_{\mathbf{R}l})(z - C_{\mathbf{R}l})}, \tag{4.2.2a}$$

$$\lambda^{\alpha}_{\mathbf{R}l}(z) = \frac{\gamma_{\mathbf{R}l} - \alpha_{\mathbf{R}l}}{\Delta_{\mathbf{R}l} + (\gamma_{\mathbf{R}l} - \alpha_{\mathbf{R}l})(z - C_{\mathbf{R}l})}, \tag{4.2.2b}$$

$$\mu^{\alpha}_{\mathbf{R}l}(z) = \frac{\sqrt{\Delta_{\mathbf{R}l}}}{\Delta_{\mathbf{R}l} + (\gamma_{\mathbf{R}l} - \alpha_{\mathbf{R}l})(z - C_{\mathbf{R}l})}. \tag{4.2.2c}$$

Note that the Hamiltonian has no explicit dependence on the screening constant α, so directly calculating Green's functions will be computationally expensive. This can be resolved by introducing a so-called auxiliary Green's function [43] that introduces the α-dependence:

$$g^{\alpha} = \left[P^{\alpha}(z) - S^{\alpha}\right]^{-1}. \tag{4.2.3}$$

One achieves a significant computational advantage when calculating g^{α} before obtaining the corresponding physical Green's function from g^{α}:

$$G_{\mathbf{R}L,\mathbf{R}'L'}(z) = \lambda^{\alpha}_{\mathbf{R}L}(z)\,\delta_{\mathbf{R}L,\mathbf{R}'L'} + \mu^{\alpha}_{\mathbf{R}L}(z)\,g^{\alpha}_{\mathbf{R}L,\mathbf{R}'L'}\,\mu^{\alpha}_{\mathbf{R}'L'}(z). \tag{4.2.4}$$

The calculations of the Green's functions are somewhat lengthy, so we refer to Ref. [43] for the computational details. Here, we will just list the final forms of the representation of NEGF in the TB-LMTO-ASA framework.

Defining $\Gamma^{\alpha}_{l/r}$ in the α-representation [17] as

$$\Gamma^{\alpha}_{l/r} = \Sigma^{\alpha,A}_{l/r} - \Sigma^{\alpha,R}_{l/r}, \tag{4.2.5}$$

the lesser self-energy $\Sigma^{\alpha,<}$ can be written as

$$\Sigma^{\alpha,<} = f_l(E)\,\Gamma^{\alpha}_{l} + f_r(E)\,\Gamma^{\alpha}_{r}. \tag{4.2.6}$$

The auxiliary Green's function in the central region $g^{\alpha,<}$ is then given by

$$g^{\alpha,<} = g^{\alpha,R}\,\Sigma^{\alpha,<}\,g^{\alpha,A}, \tag{4.2.7}$$

after which we can express the lesser Green's function in the center region as

$$G^{<}(E) = \mu^{\alpha}_{c}(E^{+})\,g^{\alpha,<}\,\mu^{\alpha}_{c}(E^{-}). \tag{4.2.8}$$

The final form for the transmission is given as

$$T(E) = \mathrm{Tr}\left[\Gamma_l^{\alpha}\, g^{\alpha,R}\, \Gamma_r^{\alpha}\, g^{\alpha,A}\right]. \tag{4.2.9}$$

These expressions were derived in Ref. [17] and we refer interested readers to it.

So far, we have outlined the implementation of NEGF in the TB-LMTO-ASA framework. The difference compared to standard DFT is that instead of the wave function ϕ_i, the Green's function is calculated and used to compute the electron density according to Eq. (4.1.10). As opposed to conventional DFT which is only valid for equilibrium situations, we now use non-equilibrium statistics to describe the states and NEGF-DFT thus allows us to study systems under finite bias and during current flow. It is extremely important to realize that the "DFT" in NEGF-DFT is actually a self-consistent field theory at nonequilibrium, because the density matrix entering the DFT functionals is constructed at nonequilibrium, and as such no variational principles exist in NEGF-DFT. In recent years, the theoretical foundation of the NEGF-DFT formalism have been put on solid form by several authors [44, 45].

4.3 The coherent potential approximation

So far in the literature of first principles quantum transport theory, assumptions are often made that the device in question is structurally perfect and has no impurities. In the real world however, there will always be imperfections in many different forms such as impurities, defects, dislocations, and so on. These imperfections can happen anywhere in the lattice, and they significantly affect quantum properties of the device. Therefore, a major part of understanding how a device works in realistic settings is the study of the effects of random disorder on quantum transport.

Up to now, effects of substitutional disorder have been studied the most and this type of disorder will also be the focus of this thesis. Substitutional disorder, also called doping in the case of semiconductors, occurs when an atom in a perfect crystal gets replaced by an impurity atom of a different type. This brings a change in the potential and charge distribution close to the impurity site, influencing the behavior of electrons moving nearby. It may also induce a structural change in the lattice if the difference between the original and impurity atom is large enough. Another effect due to differences in atomic size and chemical properties is that the impurity atom might not prefer to sit at the host atom's original site. While these effects are important on their own and are widely studied topics in the communities of electronic and mechanical structure theory, their effects on quantum transport have not been investigated to any satisfaction from atomic first principles due to lack of viable computation methods. In the rest of this thesis, we shall focus on electron disorder scattering effects to quantum transport. In order to avoid unnecessary complications, we shall neglect any structural changes due to impurity atoms and assume that the crystal structure remains unchanged. In addition, we shall assume that the impurities occur in a random fashion.

When there is random disorder, physical results must be averaged over all possible configurations of the randomness. The simplest way to do this is by brute force: generating many disordered systems for a given disorder concentration, calculating each system and then average the outcomes. This method is prohibitively expensive to use in atomic modeling. A much better way for disorder averaging is to carry out configurational averages analytically, then compute the resulting formulae just once. In particular, for the NEGF-DFT method, we shall directly average over the Green's functions that represent these physical quantities. As it will be shown, this is not simply replacing the Green's functions with their averaged values, as in general, the average of a product is not equal to the product of the averages. We will need to carefully split up the products into two separate terms which will represent the two physical contributions arising from disorder scattering.

$$\mathbf{g}(z) \to \overline{\mathbf{g}}(z), \tag{4.3.1}$$

$$G(z) \to \overline{G}(z) \ . \tag{4.3.2}$$

By doing so, we can obtain true statistically averaged quantities that are non-random. Most important is the fact that the averaged Green's functions retain the full symmetry of the underlying ideal lattice, restoring translational invariance and thus making the problem solvable again.

Consider a binary disorder consisting of two different atomic elements A and B which are distributed randomly over sites $\mathbf{R}$ with probabilities $c^A_{\mathbf{R}}$ and $c^B_{\mathbf{R}} = 1 - c^A_{\mathbf{R}}$. The MT potential of (3.2.2) can be written as a combination of both contributions:

$$V_{MT}(r_R) = \eta^A_{\mathbf{R}} V^A_{MT}(r_R) + \eta^B_{\mathbf{R}} V^B_{MT}(r_R), \tag{4.3.3}$$

where $\eta^Q_{\mathbf{R}} = 1$ if site $\mathbf{R}$ is occupied by an atom of type $Q \in \{A, B\}$ and zero otherwise. This breaks the full translational symmetry by adding statistical quantities and therefore greatly complicates the required calculations.

The disorder averaging at the single particle level, Eq. (4.3.2), will be carried out by the coherent potential theory (CPA) which is a well established method in the literature [46]. A very brief outline will be given below on CPA and its important extension, the non-equilibrium vertex correction (NVC) theory. The theory of CPA-NVC was first reported in Ref. [16] and for more details, we refer to Ref. [16, 17].

The coherent potential approximation [46, 47, 48] is applied to calculate the averaged auxiliary Green's function $\overline{\mathbf{g}}^\alpha$. It provides a self-consistent method to reduce the Hamiltonian with disorders to a translationally invariant effective Hamiltonian. CPA rewrites the average of $\mathbf{g}^\alpha(z)$, $\overline{\mathbf{g}}^\alpha(z) = \overline{[P^\alpha - S^\alpha]^{-1}}$ in terms of the coherent potential function $\mathcal{P}^\alpha$, defined as $\overline{\mathbf{g}}^\alpha = [\mathcal{P}^\alpha - S^\alpha]^{-1}$. It can be shown [17] that the coherent potential function satisfies the relation

$$\mathcal{P}^{\alpha}_{\mathbf{R}} = \overline{P}^{\alpha}_{\mathbf{R}} + (\mathcal{P}^{\alpha}_{\mathbf{R}} - P^{\alpha,A}_{\mathbf{R}})\,\overline{\mathbf{g}}^{\alpha}\,(\mathcal{P}^{\alpha}_{\mathbf{R}} - P^{\alpha,B}_{\mathbf{R}}), \tag{4.3.4}$$

which must be solved self-consistently. After introducing a T-matrix which contains all the disorder scattering information as

$$\mathbf{g}^{\alpha} = \overline{\mathbf{g}}^{\alpha} + \overline{\mathbf{g}}^{\alpha}\,\mathbf{T}\,\overline{\mathbf{g}}^{\alpha}, \tag{4.3.5}$$

the configurational average over the non-equilibrium auxiliary lesser Green's function can be written as

$$\begin{aligned} \overline{\mathbf{g}}^{\alpha,<}(z) &= \overline{\mathbf{g}^{\alpha,\mathcal{R}}\,\Sigma^{\alpha,<}\,\mathbf{g}^{\alpha,\mathcal{A}}}, \\ &= \overline{\mathbf{g}}^{\alpha,\mathcal{R}}\,\Sigma^{\alpha,<}\,\overline{\mathbf{g}}^{\alpha,\mathcal{A}} + \overline{\mathbf{g}}^{\alpha,\mathcal{R}}\,\Omega^{\alpha}_{\mathrm{NVC}}\,\overline{\mathbf{g}}^{\alpha,\mathcal{A}}, \end{aligned} \tag{4.3.6}$$

where the first term is the CPA term describing the specular transmission, and

$$\Omega^{\alpha}_{\mathrm{NVC}} = \overline{\mathbf{T}^{\mathcal{R}}\,\overline{\mathbf{g}}^{\alpha,\mathcal{R}}\,\Sigma^{\alpha,<}\,\overline{\mathbf{g}}^{\alpha,\mathcal{A}}\,\mathbf{T}^{\mathcal{A}}} \tag{4.3.7}$$

is the non-equilibrium vertex correction term describing diffusive scattering. This term has been neglected up to now. However, it is to be shown both in this thesis and in other works [33, 34, 49, 50] that this quantity can play a major role in determining the transport properties of disordered systems, justifying its use. The full derivation of this quantity $\Omega^{\alpha}_{\mathrm{NVC}}$ was originally done in Ref. [17]. It can be shown [16] that the total averaged transmission is the sum of two contributions:

$$\overline{T}(E) = \mathrm{Tr}\left[\Gamma_l\overline{\mathbf{g}}^{\alpha,\mathcal{R}}\Gamma^{\alpha}_r\overline{\mathbf{g}}^{\alpha,\mathcal{A}}\right] + \mathrm{Tr}\left[\Gamma^{\alpha}_l\overline{\mathbf{g}}^{\alpha,\mathcal{R}}\Omega'_{VC}\overline{\mathbf{g}}^{\alpha,\mathcal{A}}\right], \tag{4.3.8}$$

where the first term stands for the specular term obtained from CPA, and the second term is the vertex correction (VC) term, describing diffusive scattering. The quantity Ω'_{VC} is obtained from the expression of Ω_{NVC} by replacing $\Sigma^{\alpha,<}$ with Γ^{α}_r in Eq. (4.3.7).

4.4 Summary

In this chapter, we have given a review of the LMTO method. In its selfconsistent tight-binding form and atomic sphere approximation (TB-LMTO-ASA) form, it is very efficient in computing very large systems of atoms. We then introduced the non-equilibrium Green's function formalism, allowing us to use Green's functions to calculate physical quantities instead of using conventional wavefunction-based formalisms. This gives us several benefits, and by far the most important ones are the ability to do quantum statistics in a non-equilibrium setting, and to systematically include disorder in the calculation. The first one allows us to do quantum transport calculations as these problems are intrinsically under a non-equilibrium, finite voltage bias. We have shortly outlined the second advantage in the form of CPA-NVC, allowing us to calculate configurational averages of Green's functions to allow us to calculate electronic properties in systems with substitutional disorder without resorting to brute-force methods. In the next chapter, we will apply these methods to the research topic of this thesis: disordered graphene.

5

Quantum transport in graphene

Using the theoretical framework of LMTO-CPA-NVC within NEGF-DFT reviewed in the last three Chapters, we are ready to investigate quantum transport properties of disordered graphene. The two-probe device is shown in Fig. 5.1, where left and right leads extend to infinitely far. In this two-probe device model, the leads are assumed to be perfect graphene without disorder, and disorder resides in the device region. The NEGF-DFT self-consistent calculation is carried out for atoms in-between the left and right leads, namely those in the two buffer layers and device region as indicated in Fig. 5.1. The buffer layers are perfect graphene and their purpose is to screen any possible interaction the device region may have with the electronic structure of the leads. When the buffer layers are thick enough, the electronic potential at the boundaries of the buffer layers and the leads will match perfectly. Such a screening approximation has been well established in literature [38], allowing us to focus on the transport physics of the device region. On the other hand, the influence of the semi-infinite leads to the device region is fully included through the self-energies $\Sigma^{r,a}$ discussed in Chapter 4. These self-energies are calculated precisely using the surface Green's function technique reported in Ref. [51]. The two-probe device model shown in Fig. 5.1 is thus solved within NEGF-DFT in a computational box that includes vacuum regions above and below the graphene.

In this Chapter, after carefully building the ASA model for graphene and verifying the electronic structure of pristine systems, we shall investigate effects of substitutional boron (B) and nitrogen (N) doping in a graphene device connected to intrinsic

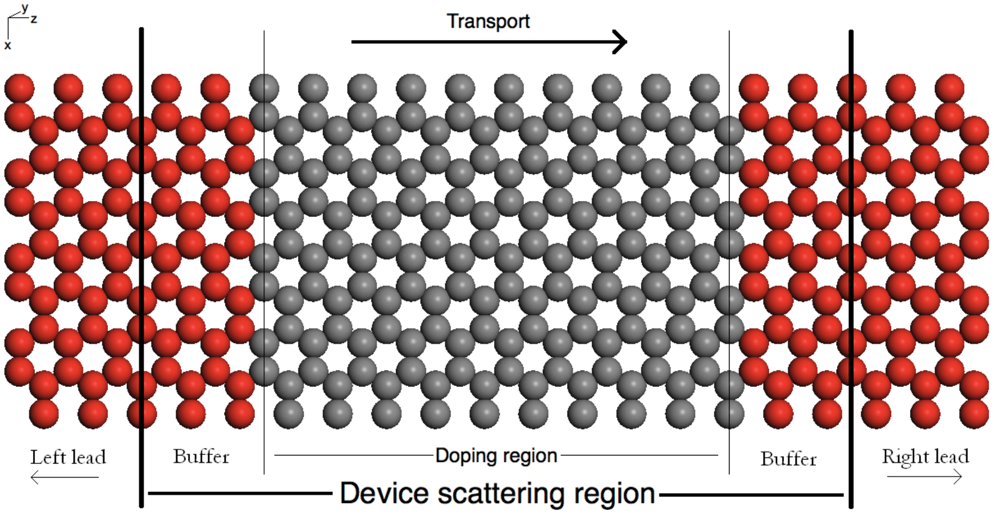

Figure 5.1: A sketch of the graphene two-probe configuration. The transport is taken to be in the zigzag, z-direction. The graphene sheet is infinitely long in the x-direction, and the graphene images are periodic in the out-of-plane y-direction separated by a large distance of 8.93 Å. Typical device lengths are 4.9 nm to 19.6 nm.

graphene electrodes. A particular technical issue is how to set up the atomic sphere approximation (ASA) for the vacuum region. We have calculated quantum transport of two-probe graphene devices versus the disorder concentration x, the device length L, the electron electron energy E, and our first principles results suggest that impurity doping greatly affects quantum transport properties by inducing significant diffusive scattering. The NVC theory of the last Chapter allows us to directly determine the diffusive scattering contribution to the total conductance. Since boron and nitrogen atoms are located on either side of carbon in the periodic table, a very interesting finding is that disorder scattering due to these impurities mirror almost perfectly on either side of the graphene Fermi level. Such a behavior can be understood from the point of view of charge doping.

5.1 The ASA model for graphene

Our atomic sphere approximation (ASA) within LMTO used for graphene is inspired by the model for graphite reported in Ref. [52]. Considering the symmetry of graphene, we built various sphere configurations and tested them very carefully.

The issue is how to fill the vacuum regions with empty spheres so that ASA gives an accurate electronic structure. We chose the atomic spheres to be AA-stacking to preserve the six-fold symmetry of graphene.

The NEGF-DFT numerical calculation is done in a computational box containing the two probe graphene device shown in Fig. 5.1 where the transport direction is along the z-axis. The graphene device is a film (thus periodic) along the x-axis, and three vacuum regions are included between the graphene regions along the y-axis. With thick vacuum regions, the y-direction can also be treated as periodic since the vacuum prevents periodic images from interacting with each other. In our calculation, the total vacuum thickness in the computation box is $d = 8.93\,\text{Å}$. Looking at the electrostatic dipole interactions between the layers we could observe that they dropped to negligible values starting at this thickness. In this way, there is essentially no interaction between the periodic images, thus simulating a single graphene layer. Because our NEGF-DFT is implemented in LMTO which is an atomic center based method, the vacuum region must be filled with empty spheres. Our computation box (the unit cell shown in Fig. 5.2) thus contains one layer of graphene plus three additional layers of empty spheres to simulate vacuum (labelled VAC).

To preserve the symmetry of the system, we locate the empty spheres on coordinates of the graphene carbon sites. We put large empty spheres (labelled VA) at the remaining points of symmetry to fill up the remaining volume. As mentioned in section 3.7, these empty spheres have no physical meaning but are required to make the geometry close packed in order to improve the accuracy of ASA. Detailed information on the geometry is shown in Fig. 5.2 and Table 5.1. The primitive unit cell has 12 atomic spheres in total.

The LMTO calculations are done using an *spd*-basis set so there are nine orbitals per atomic site. For the Brillouin zone (BZ) integration, we take the special points of BZ into account and have made sure that both the Γ- and K-points are included in our k-sampling mesh. As mentioned before and shown in Fig. 5.2, the unit cell

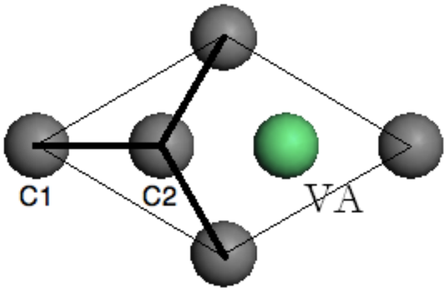

(a) Top view

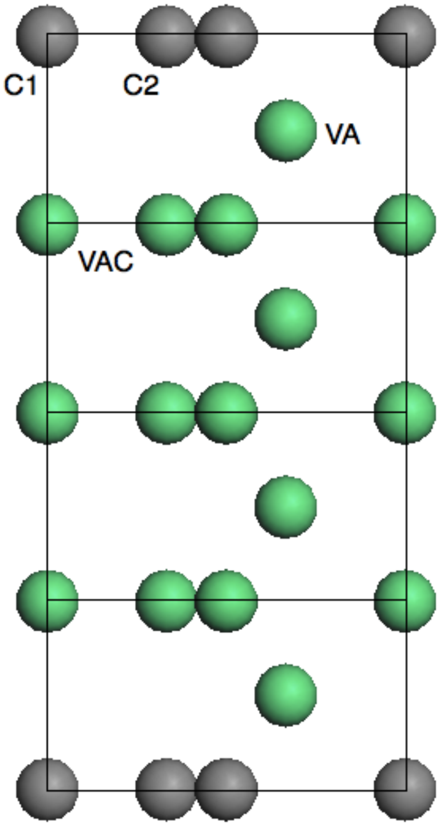

(b) Side view

Figure 5.2: The primitive cell of graphene with empty spheres. (a) is the top view and (b) is the side view. In (b) enough vacuum regions have been added to make sure that the graphene images do not interact with each other.

consists of a slab where a vacuum region is put to separate the images of the graphene layer to form a supercell that is periodically extended along the out-of-plane direction. Since the vacuum regions are thick enough so that the images of the graphene layer do not interact in the out-of-plane direction, only a single k-point is needed for the

Atom	Position	Sphere radius (a.u.)
C_1	$(0,0,0)$	1.59
C_2	$(\frac{2}{3},\frac{2}{3},0)$	1.59
VA	$(\frac{1}{3},\frac{1}{3},\frac{1}{8})$	2.20
VAC_1	$(0,0,\frac{2}{8})$	1.59
VAC_2	$(\frac{2}{3},\frac{2}{3},\frac{2}{8})$	1.59
VA	$(\frac{1}{3},\frac{1}{3},\frac{3}{8})$	2.20
VAC_1	$(0,0,\frac{4}{8})$	1.59
VAC_2	$(\frac{2}{3},\frac{2}{3},\frac{4}{8})$	1.59
VA	$(\frac{1}{3},\frac{1}{3},\frac{5}{8})$	2.20
VAC_1	$(0,0,\frac{6}{8})$	1.59
VAC_2	$(\frac{2}{3},\frac{2}{3},\frac{6}{8})$	1.59
VA	$(\frac{1}{3},\frac{1}{3},\frac{7}{8})$	2.20

Table 5.1: Atomic centers and radii for the primitive unit cell in the ASA approximation. Positions are given in terms of the lattice vectors. The in-plane lattice vectors are given by $\mathbf{a}_1 = a\,(\frac{\sqrt{3}}{2},\frac{1}{2},0), \mathbf{a}_2 = a\,(\frac{\sqrt{3}}{2},-\frac{1}{2},0)$, and the out of plane lattice vector is $\mathbf{a}_3 = b\,(0,0,\frac{8}{6})$, where $a = 2.45\,\text{Å}$ is the graphene lattice constant, and $b = 6.7\,\text{Å}$ is the graphite out of plane constant. There are 2 different empty spheres denoted by VA and VAC. The spheres denoted by VA are the empty spheres between the graphene layers, whereas VAC stand for empty spheres in the place of a carbon sphere.

out-of-plane k-sampling.

For the remaining two dimensional (2D) BZ, we use a uniform k-point distribution, dividing the BZ into equal parallelograms and putting the k-sampling points at the corners of the parallelograms, instead of putting them in the middle as is done conventionally. Weights are adjusted accordingly. At the edge of the BZ, the weight of the k-sampling point is 2; at the four corners of the BZ, the weight is 1; at all other locations, the weight is 4. This scheme ensures that the Γ-point is included in the calculation. To include the special Dirac points, we put k-sampling points at one-third and two-thirds of the BZ, as shown in Fig. 5.3. This means that if we distribute k-sampling points from $k = -N_k$ to $k = N_k$, N_k has to be divisible by three. The total number of k-sampling points for the full BZ equals to $k_{\text{total}} = (2N_k + 1)^2$. For equilibrium situations there is time-reversal symmetry so we can calculate for just one half of the BZ and then map the result onto the other half, reducing computational effort by a factor of two. In our calculations, we use $N_k = 30$, giving us a $61 \times 31 \times 1$ grid in the k-sampling mesh. Increasing the number of k-points by doubling N_k did not change the Fermi energy at all, so we took $N_k = 30$.

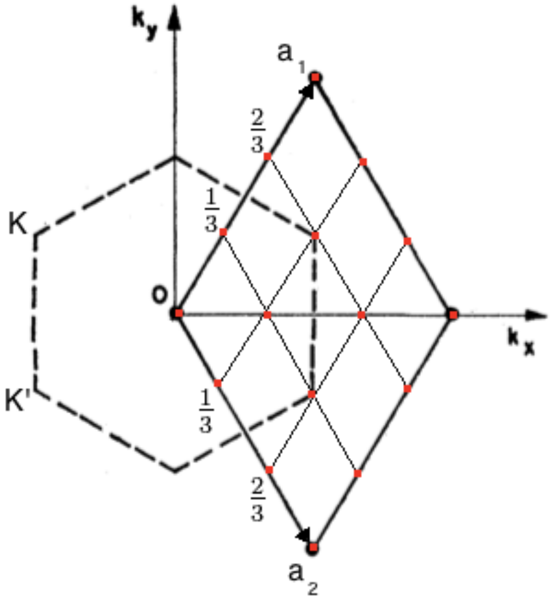

Figure 5.3: A schematic of the k-sampling mesh of the Brillouin zone of graphene. k-points (shown as red dots) are equally spaced along the lattice vectors $\mathbf{a}_1$ and $\mathbf{a}_2$, producing a uniform mesh. In order to include the K and K' Dirac points as shown in the diagram, we need to include points at one-thirds and two-thirds of the lattice vectors.

Two-probe calculations consist of dividing the device into principal layers along the transport direction (z-direction). These principal layers should be thick enough so that each layer only interacts with its left and right neighboring layers [38]. In this way, the Hamiltonian matrix H_0 in Eq. (4.1.6) will be tridiagonal and the resulting expression can be inverted efficiently to obtain the Green's function. In order to divide the two-probe device into principal layers it is necessary to use a rectangular unit cell with one lattice vector along the transport direction (z-direction) and the other vectors perpendicular to it. This rectangular unit cell has twice the size of the primitive cell shown in Fig. 5.2.

We observed that k-sampling was much more complicated for the rectangular unit cell, and as such we needed to use a grid of $421 \times 31 \times 1$ to accurately compute the Fermi energy of the leads. In the NEGF-DFT self-consistent calculations, k-sampling is done in the 2D BZ in the x-y directions with 31 × 1 k-sampling points. After self-consistency has been achieved between the Hamiltonian and density matrix (i.e. the NEGF-DFT is converged), we calculate the transmission coefficient $T(E)$ using Eq. (4.3.8). The k-sampling in the $T(E)$ calculation requires a larger mesh to converge, and we found that a 601 × 1 mesh was necessary for this calculation.

We chose the zigzag-direction of the graphene as the transport direction (z-direction), since the zigzag-direction has a higher transmission rate than the armchair direction [53]. The aforementioned principle layer is taken as a single graphene hexagon with a length equal to the lattice constant $a = 2.45\,\text{Å}$. Each principle layer consists of 24 atomic spheres. The device lengths studied here are between 5 principle layers (1.23 nm) and 40 principle layers (9.8 nm), however it is possible [18] to increase this length to over 80 principle layers (19.6 nm). To find out how many buffer layers we need to include in the center region for screening purposes, we investigate how good the electrostatic potential converges to the bulk value at the end of the buffer region. Unfortunately, for intrinsic graphene electrodes, a buffer region of at least 24 principle layers is required. Hence, a total of 48 principle layers of graphene are included in the device region just for screening purposes. In other words, graphene does not screen interaction very well which is a typical behaviour for low dimensional systems. In summary, the two-probe devices of Fig. 5.1 contain 1272 to 2112 atomic spheres in the NEGF-DFT calculation, for 1.23nm and 9.8nm device lengths respectively.

5.2 Perfect graphene

We first study the case of perfect graphene and investigate whether the LMTO-ASA method can produce accurate results for such a system that has received extensive theoretical investigations in literature. The energy windows we look at are $[-5, 5]$ eV for density of states (DOS) calculations, and $[-1.36, 1.36]$ eV for transmission $T(E)$ calculations.

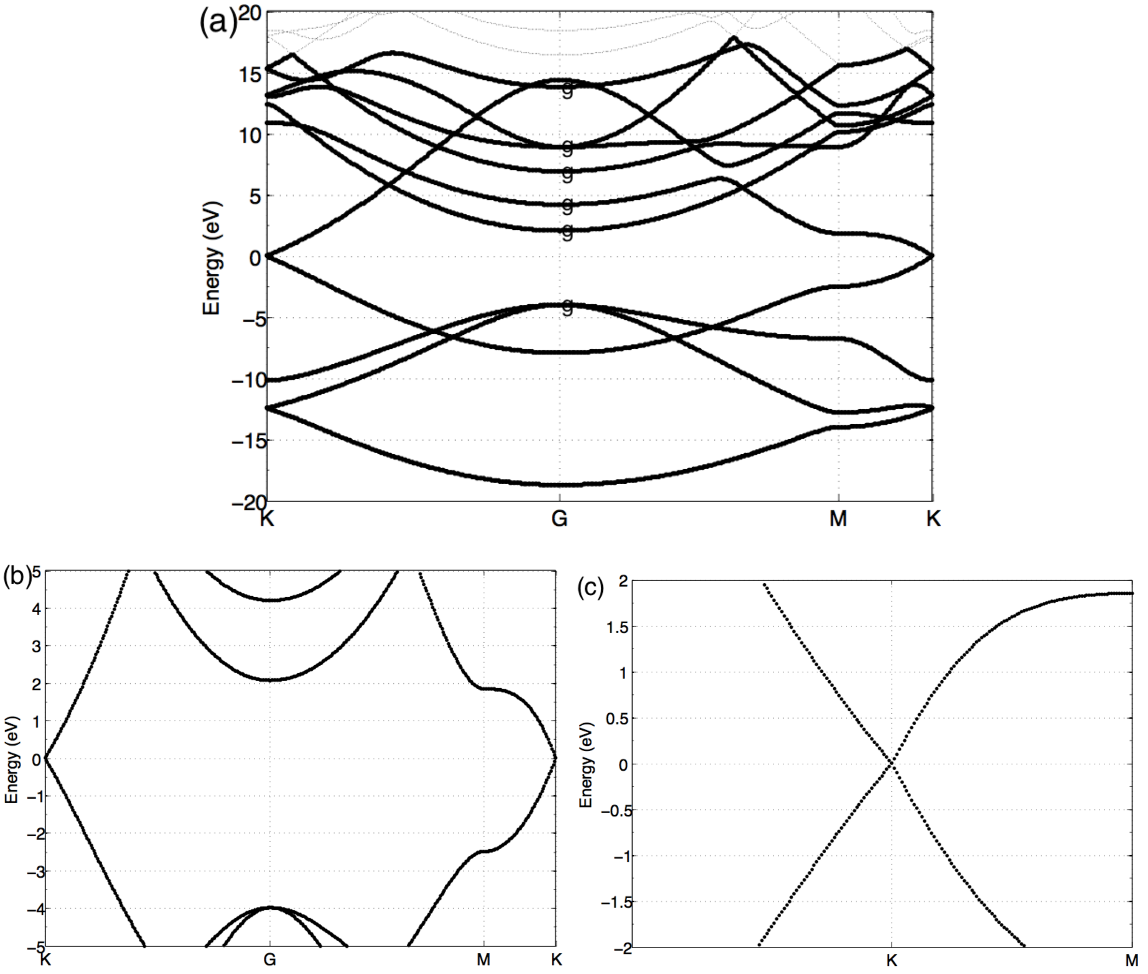

Figure 5.4: Band structure of perfect graphene, for (a) a large $[-20, 20]$ eV window, in the K-Γ-M-K direction; (b) a smaller, $[-5, 5]$ eV window in the same BZ direction; (c) a $[-2, 2]$ eV window centered around the Dirac K-point, in the halfway-Γ-K-M BZ direction. The ghost bands, labelled in (a) by 'g', are unphysical and do not affect the quantum transport calculations in the energy window close to $\mathcal{E}_F$. In this window as shown in (c), the band structure is in excellent agreement with other first principles calculations [6].

Looking at the band structures at different energy windows of Fig. 5.4, we note the following. There are some bands that do not appear in plane wave DFT calculations, these are the so called "ghost bands" arising from the atomic sphere approximation. These bands however do not come into play in the energy window of $[-1.36, 1.36]$ eV surrounding the Fermi level which is the relevant energy range of transport. Indeed, experimental measurements of conductance are done at the Fermi level. At the Dirac K-point, we can see a kink in the band structure, this is to be expected as the slope of the dispersion relation depends on the exact direction of the $\mathbf{k}$-vector.

The corresponding local density of states (LDOS) is calculated for periodic graphene, see Fig. 5.5. We have also plotted the orbital contributions to the total DOS. It is clear that the p-orbital of carbon atoms completely dominates the DOS of graphene, as expected. There appears to be a small but non-zero DOS at the Fermi energy. Since the Fermi energy of graphene cuts the Dirac point, we expect the DOS there to be zero. The reason of the small but non-zero DOS at the Fermi energy is traced back to a numerical issue. In Green's function calculations of the density matrix, Eq. (4.1.10), there are many Van Hove singularities when the denominator of Eq. (4.1.6) vanishes. These singularities are regularized by adding a small imaginary constant $i0^+$ to the denominator of Eq. (4.1.6). While 0^+ should be a positive infinitesimal, in practical calculations it takes a small but finite value. This smearing constant gives rise to the small but finite DOS at the Fermi energy.

The transmission coefficient $T(E)$ versus electron energy E is plotted in Fig. 5.6, showing a V-shaped curve going to zero at $E = \mathcal{E}_F$ in a linear manner. The V-shape corresponds perfectly to the band structure of graphene (see Fig. 5.4(c)). Indeed, for a perfect graphene device, there is no scattering and every Bloch state transmits perfectly. Hence, $T(E)$ should show a V-shape because the band structure has a V-shape. Note that the calculated $T(E)$ is also consistent with the DOS of perfect graphene (see Fig. 5.5): within the energy range of ±1.4 eV in which $T(E)$ is plotted, the DOS also has a V-shape. We conclude that the results of the ASA model of perfect graphene is in good agreement with other first principles calculations [54].

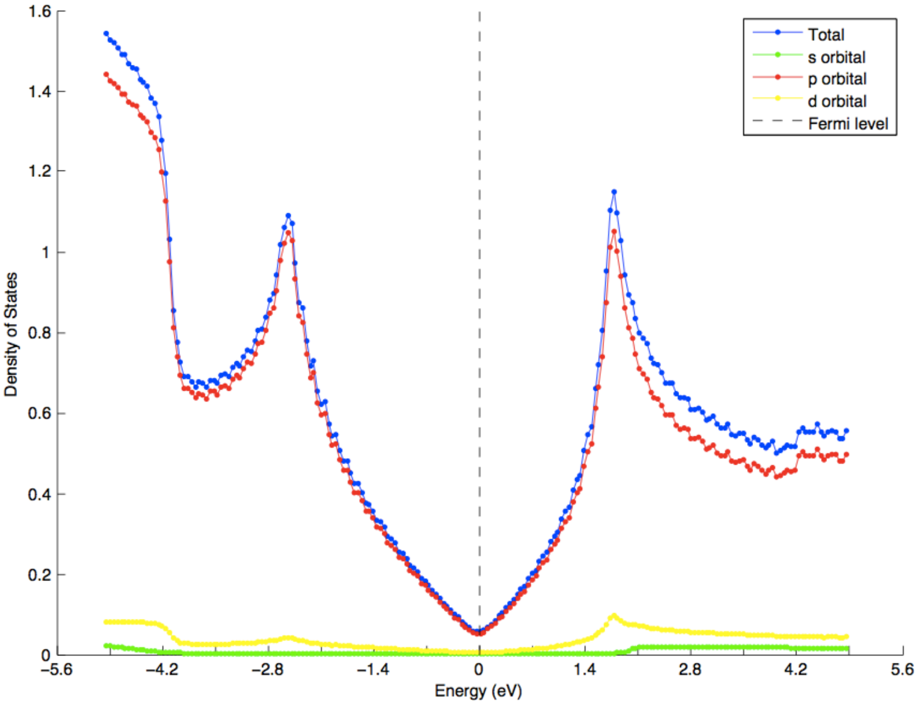

Figure 5.5: (Local) density of states of perfect graphene. Note that the DOS appears to be nonzero at $E = \mathcal{E}_F$. This is due to the smearing constant added to the integration of the DOS, making it appear smooth but also less accurate. The actual DOS is still zero at $E = \mathcal{E}_F$, which gives rise to the zero $T(\mathcal{E}_F)$ in the following graph, Fig. 5.6.

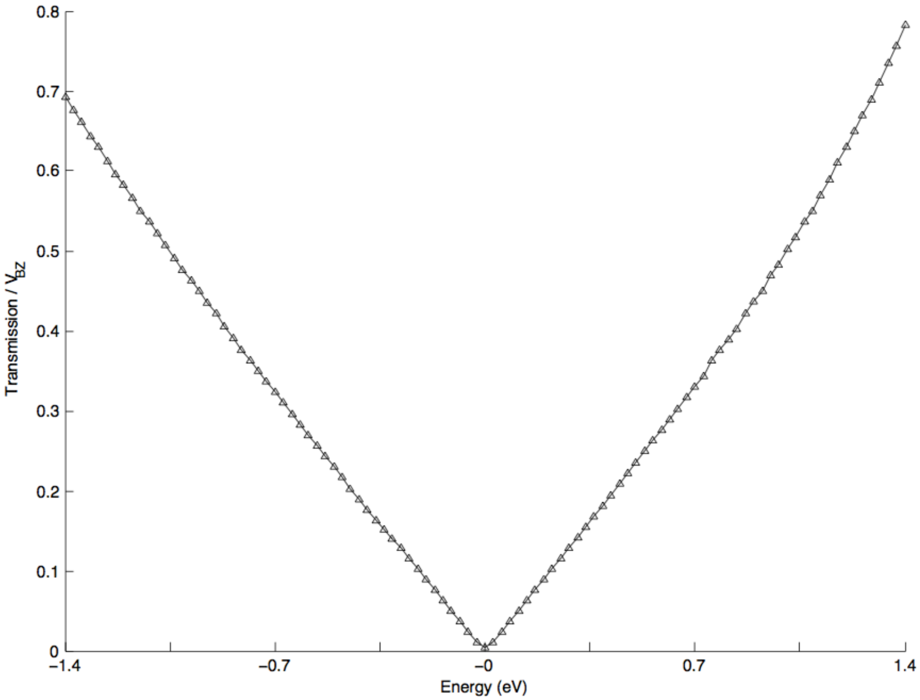

Figure 5.6: Transmission coefficient $T(E)$ versus electron energy E of perfect graphene.

5.3 Effects of disorder

We consider substitutional disorder by adding a certain fraction $x\%$ of either boron or nitrogen atoms to replace carbon atoms in the device region. As discussed in Chapter 4, the random disorder configurations are treated by the coherent potential approximation (CPA) at the single particle Green's function level. Boron and nitrogen sit to the left and right of carbon in the periodic table and are thus very similar to carbon in terms of their atomic radii and orbitals. This makes them physically easier to substitute carbon atoms in graphene. This kind of doping has been investigated on carbon nanotubes [55], and its effects on graphene have also been predicted by tight binding semi-empirical calculations [54]. Here we use a first principles method to calculate their effects on quantum transport.

A nitrogen atom is an electron donor to graphene, making it n-type doped, whereas a boron atom is an acceptor (adds a hole) which makes it p-type doped. Such charge transfers shift the Fermi energy of the graphene up or down and also change the electrostatic potential of the device. The doped impurities provide scattering centers at random locations in the device which gives rise to diffusive scattering of the electrons.

We begin by investigating the changes to the potential due to uniform impurity doping, using the CPA implemented in our LMTO software. Analogous to semiconductors, doping a device with electrons makes it n-type and will lower the potential. Doping it with holes does the exact opposite, the device will become p-type and the potential will increase. The calculated results are shown in Fig. 5.7.

The density of states gives an indication of how the transmission will behave. We calculated the local density of states (LDOS) on the C and B, N atoms, and the results are shown in Figs. 5.8(a) and 5.8(b). Comparing Fig. 5.8(a) to Fig. 5.5 of perfect graphene, the LDOS remains unchanged for carbon atoms but they are shifted with respect to the Fermi energy due to charge transfers to or from the impurity atoms. In the nitrogen case of Fig. 5.8, the Fermi energy shifts up as one would expect because

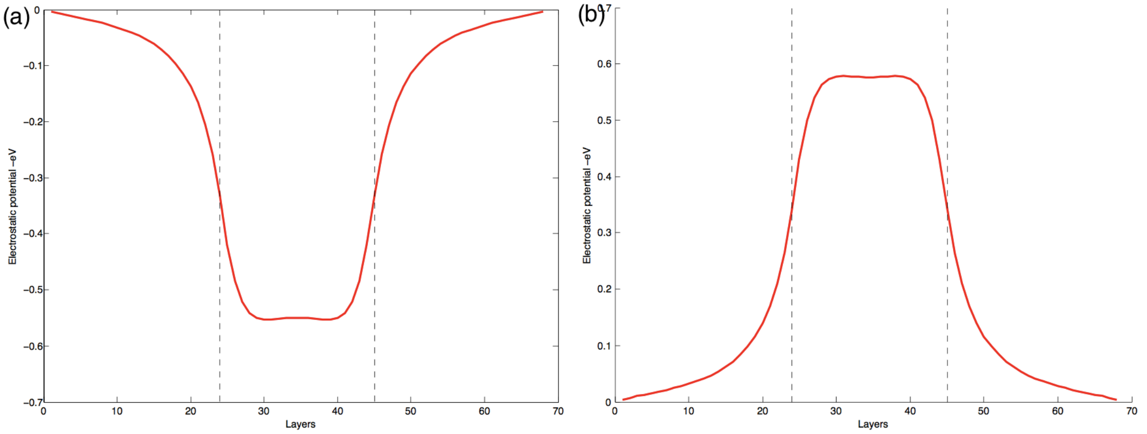

Figure 5.7: The electrostatic potential along the z-axis of a 4.9 nm two-probe device doped with (a) 1% nitrogen and (b) 1% boron. The horizontal axis is in unit of principle layers. We can see that doping creates a potential difference between the doped region and the intrinsic leads. The regions inside the dashed lines are doped, the outer regions are intrinsic graphene layers that act as screening buffers.

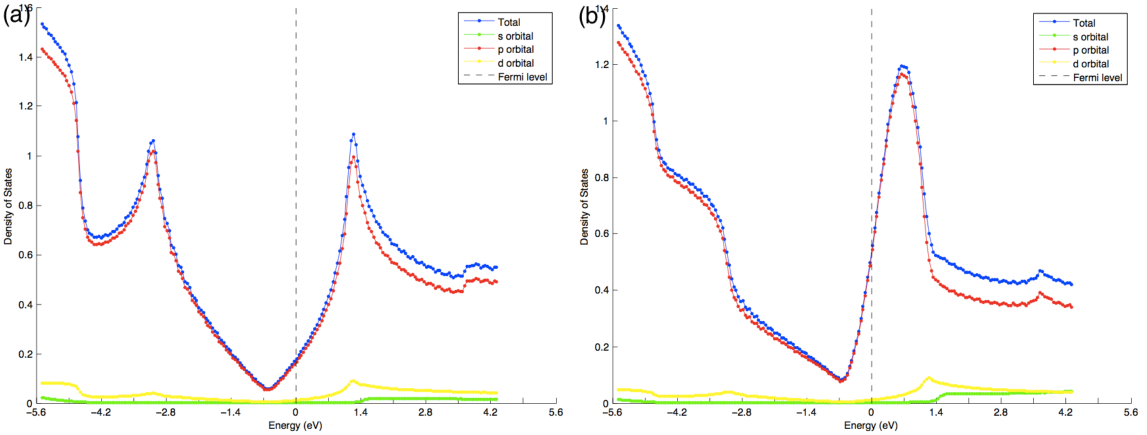

Figure 5.8: Density of states of graphene with 1% nitrogen impurities. (a) Local DOS of carbon. (b) Local DOS of nitrogen.

nitrogen transfers charge to the graphene. The LDOS for the nitrogen atom shows the typical nitrogen peak at ~ 0.7 eV, consistent with earlier calculations [54].

Analogous to adding electrons, removing electrons from graphene by boron impurities produces the reverse effect, shown in Fig. 5.9, where the Fermi energy is shifted downwards as shown in Fig. 5.9(a). The LDOS for the B atom shows a boron-peak in the opposite energy direction. Note that in the energy window of $[-1.36, 1.36]$ eV, the LDOS of B is almost identical to that of N mirrored at the Fermi energy.

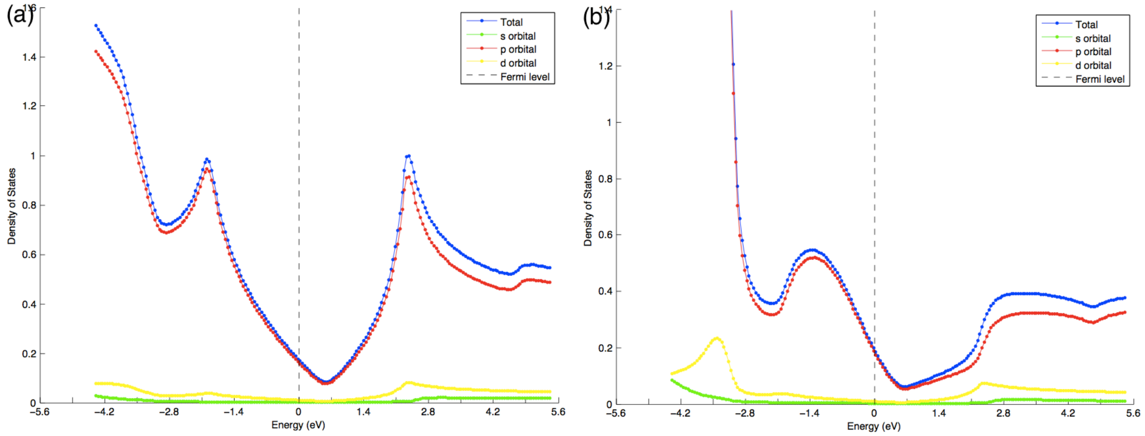

Figure 5.9: Density of states of graphene with 1% boron impurities. (a) Local DOS of carbon. (b) Local DOS of boron.

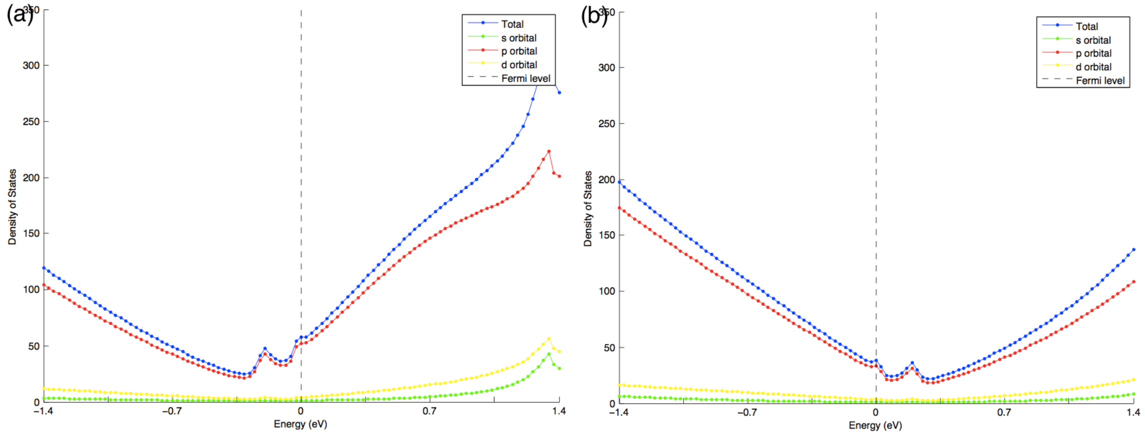

Figure 5.10: Total density of states of the center scattering region of the two-probe device. (a) Total DOS of graphene with 1% nitrogen impurities. (b) Total DOS of graphene with 1% boron impurities.

We can take all the contributions from the LDOS in the device scattering region and sum them up to obtain the total DOS (TDOS) of the entire device. The resulting plot is the combination of many different contributions. Firstly, there is the contribution of the intrinsic pure graphene (Fig. 5.5) in the scattering region of the device. Then, there are the contributions of LDOS from both the carbon (Fig. 5.8(a)) and impurity atom (Fig. 5.8(b)) in the doped graphene region, whose minima are shifted with respect to the Fermi energy. The maxima and minima we see in the plots of Fig. 5.10 are pure consequences of this sum. In particular, there appears to be a TDOS pick at -0.3eV in Fig.5.10(a) and at $+0.3$eV in Fig.5.10(b). These peaks are not due to any molecular or atomic states at those energies, but purely due to the summation of various contributions of LDOS to the TDOS.

We now show the $T(E)$ plots of various doping concentrations. We display both the transmission of intrinsic graphene and that of doped graphene, with contributions from the coherent part and the vertex correction (VC) term according to Eq. (4.3.8). Note that the first term in Eq. (4.3.8) gives the specular contribution to $T(E)$, while the second term, which is the VC term, gives the diffusive scattering contribution to $T(E)$. We begin with concentrations of 1%, 3%, and 5% in separate plots.

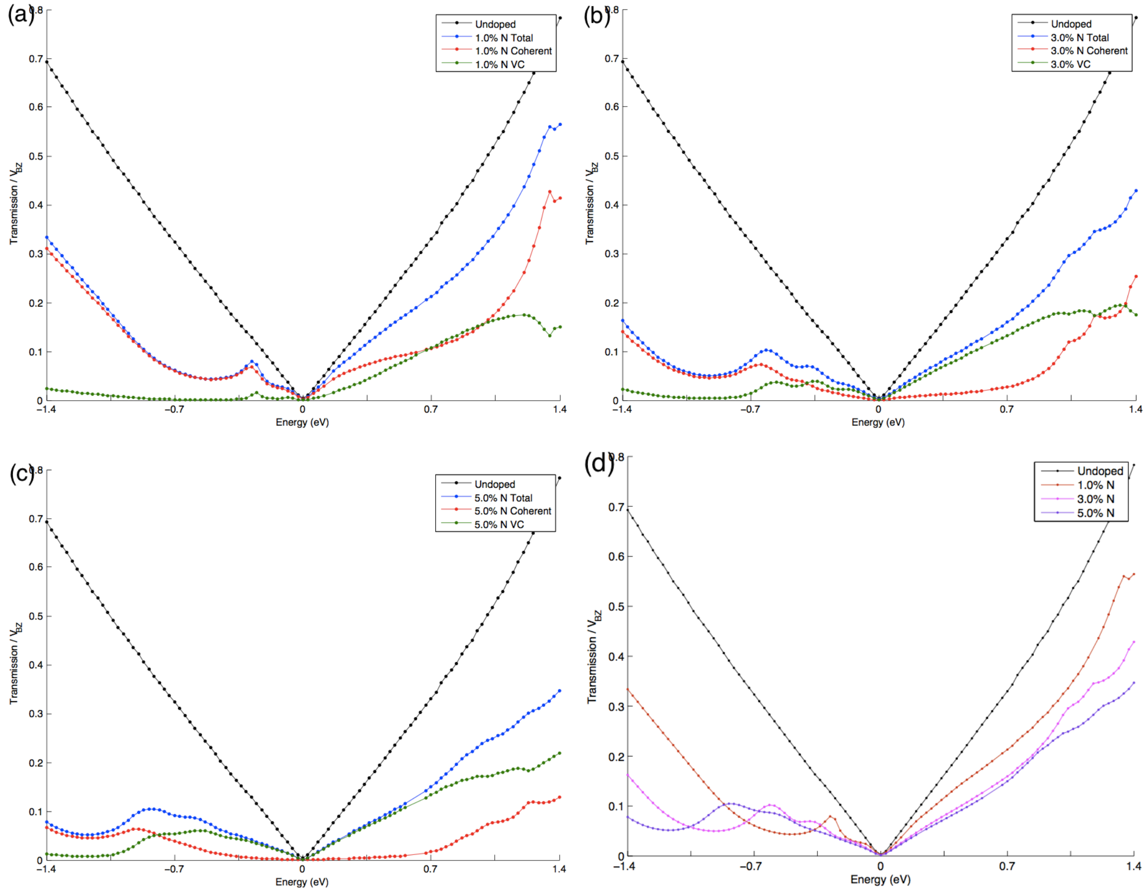

Figure 5.11: $T(E)$ of a 4.9 nm graphene device with nitrogen impurities. (a) 1% (b) 3% (c) 5% (d) 1%, 3%, and 5% on the same plot.

In the case of nitrogen doping (Fig. 5.11), we found that nitrogen impurities greatly affect $T(E)$. We observe the small peak arising from the DOS summation at around $E \sim -0.3$ eV, and a significant VC contribution around the nitrogen peak of Fig. 5.8(b), i.e. around $E \approx 0.7$eV. This makes sense physically, as the VC term in Eq. (4.3.8) describes the scattering by impurities. As the impurity concentration is increased, the Fermi energy is shifted more, hence the small transmission peak is shifted more and more to the left. It also changes shape to more and more resemble the characteristic nitrogen "bump" which is also shown in the LDOS of N (at around $E \sim 0.8$ eV in Fig. 5.8(b)). The VC term (diffusive scattering) gains more and more importance as impurity concentration increases, since there are more nitrogen atoms in the system to scatter from.

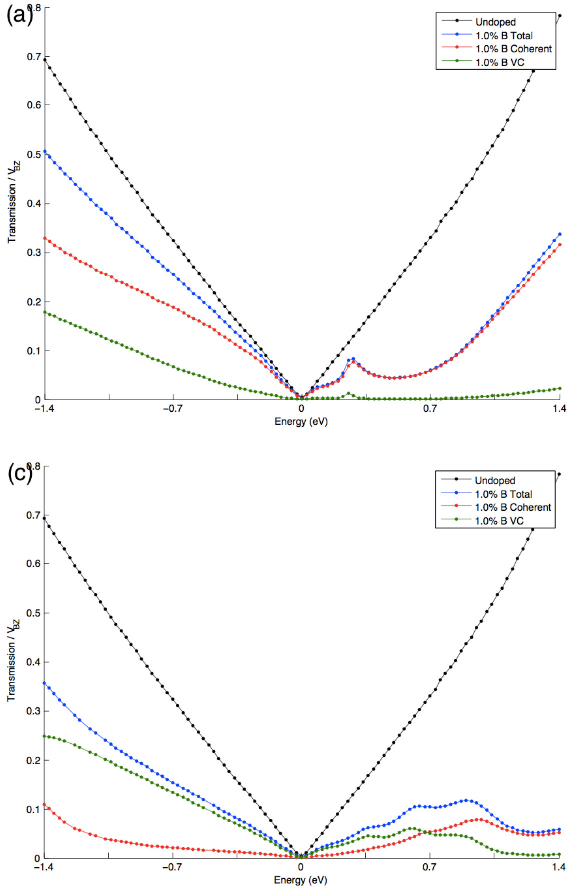

Figure 5.12: $T(E)$ of a 4.9 nm graphene device with boron impurities. (a) 1% (b) 3% (c) 5% (d) 1%, 3%, and 5% on the same plot.

For boron doping, as shown in Figs.5.12(a) to 5.12(d), we see that the effect is analogous to that of nitrogen but in the opposite energy direction. This reinforces our interpretation that these impurity effects are purely electronic, as adding an electron is electronically the opposite as adding a hole to the system.

As a short summary, we plot all the transmission coefficients at different doping concentrations concentrations in one graph, Figs. 5.13 and 5.14. These plots show very clearly how increasing the concentration enhances effects caused by impurity doping.

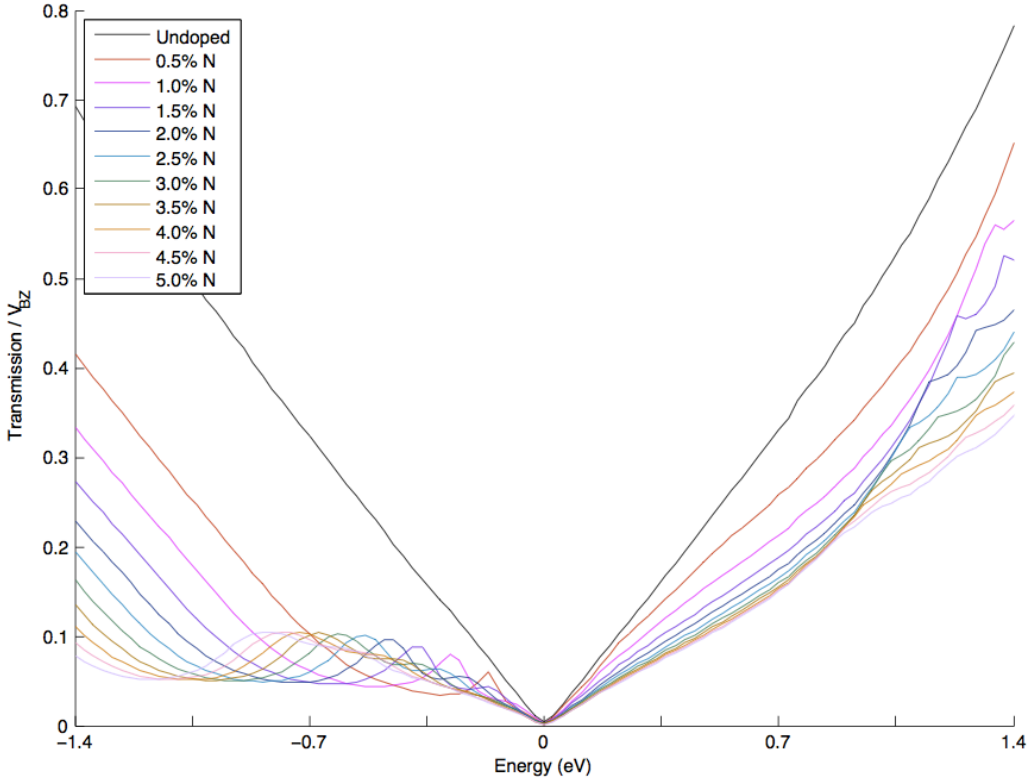

Figure 5.13: Transmission coefficient $T(E)$ of a 4.9 nm graphene device with nitrogen impurities as a function of electron energy for many doping concentrations between 0.5% and 5.0%.

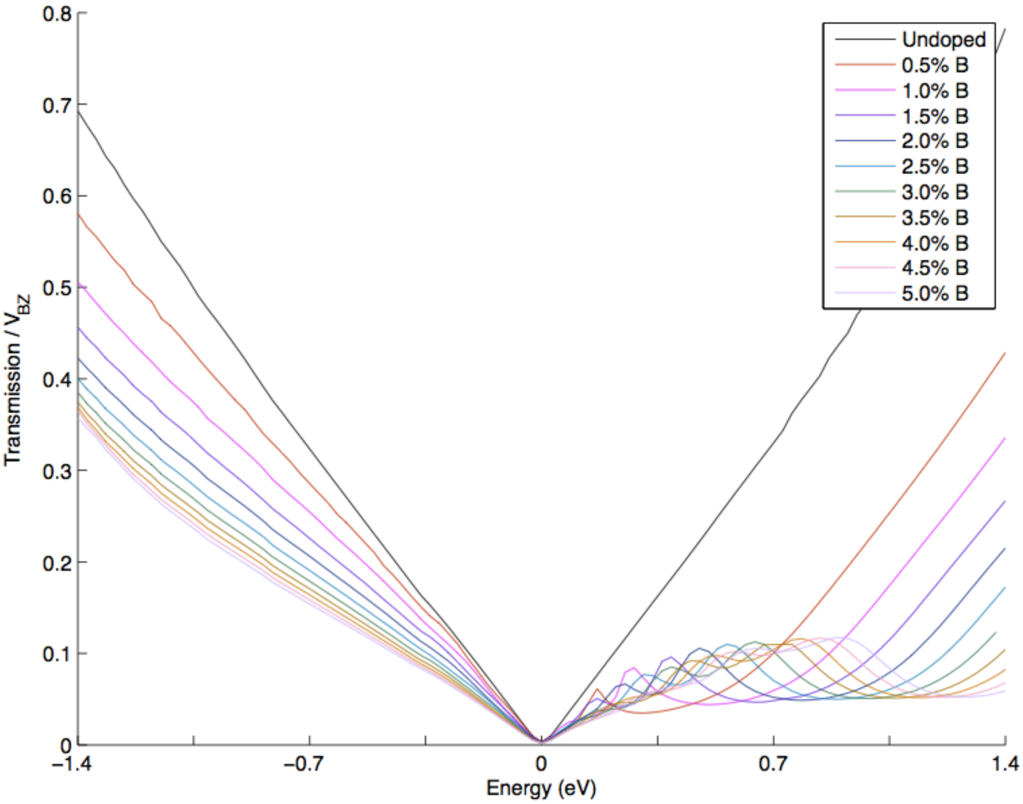

Figure 5.14: Transmission coefficient $T(E)$ of a 4.9 nm graphene device with boron impurities as a function of electron energy for many doping concentration between 0.5% and 5.0%.

We now turn to dependence of transport on the device length L which is the linear length of the scattering region of Fig. 5.1 along the transport direction, fixing the concentration at a constant 1%. Since the buffer regions of the scattering region are fixed, increasing L means increasing the doping region. Hence, a smaller L means a smaller absolute amount of impurities in the device, hence a smaller contribution by all the impurities to the device DOS. Increasing L will increase the absolute number of impurity atoms thereby increasing the impurity effects on the DOS. These features are shown in Figs. 5.15 and 5.16. In general, doping impurities reduce transmission because impurity scattering typically increases resistance. In particular, the vertex correction contribution (second term in Eq. (4.3.8)) to the transmission coefficient (blue curves) becomes more prominent in the longer device because there are more impurities to scatter from.

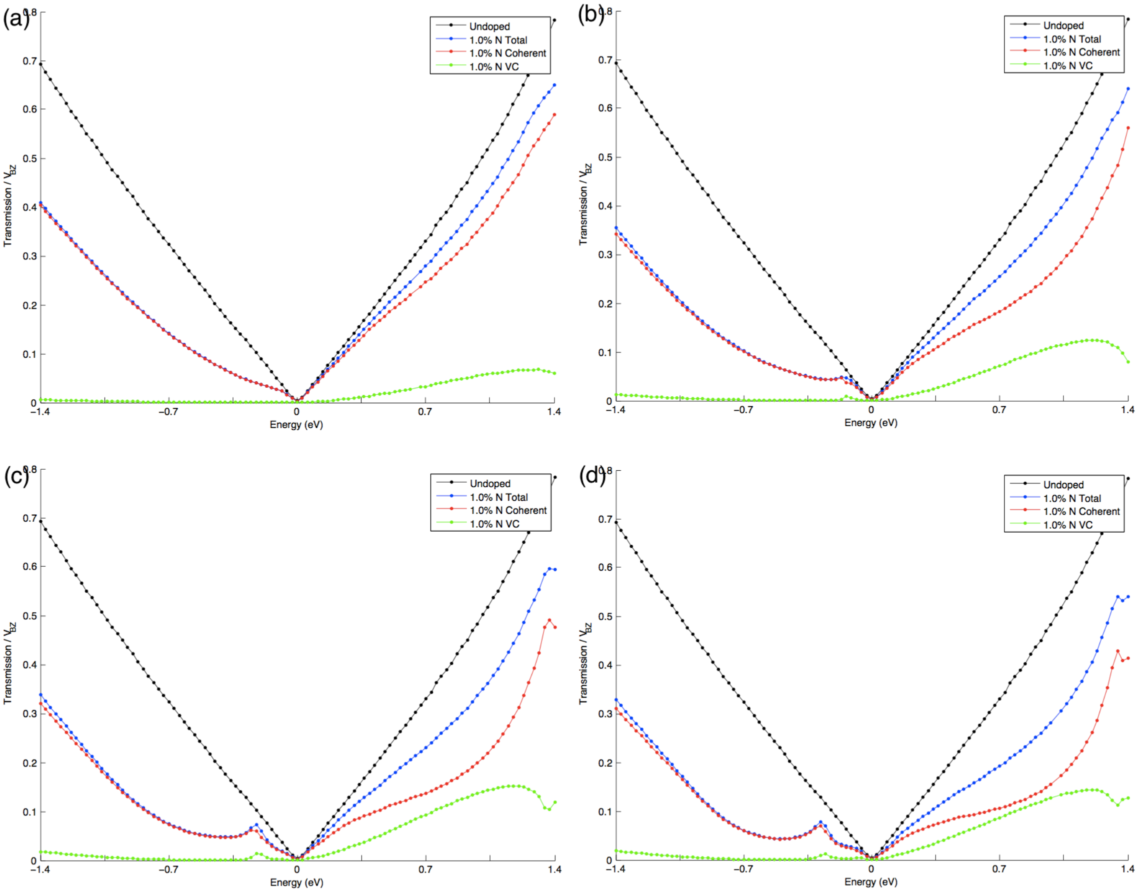

Figure 5.15: Transmission coefficient $T(E)$ versus electron energy of a graphene device with 1% nitrogen impurities. (a) Device length $L = 1.22$ nm, (b) $L = 2.45$ nm, (c) $L = 3.68$ nm, (d) $L = 4.9$ nm. The black curve is the transmission for perfect graphene without any impurity, for comparison purposes. The blue curve is the total transmission with 1% impurity. The red curve is the coherent part of the transmission (the first term of Eq. (4.3.8); and the green curve is the vertex contribution which describes the diffusive scattering, namely the second term of Eq. (4.3.8).

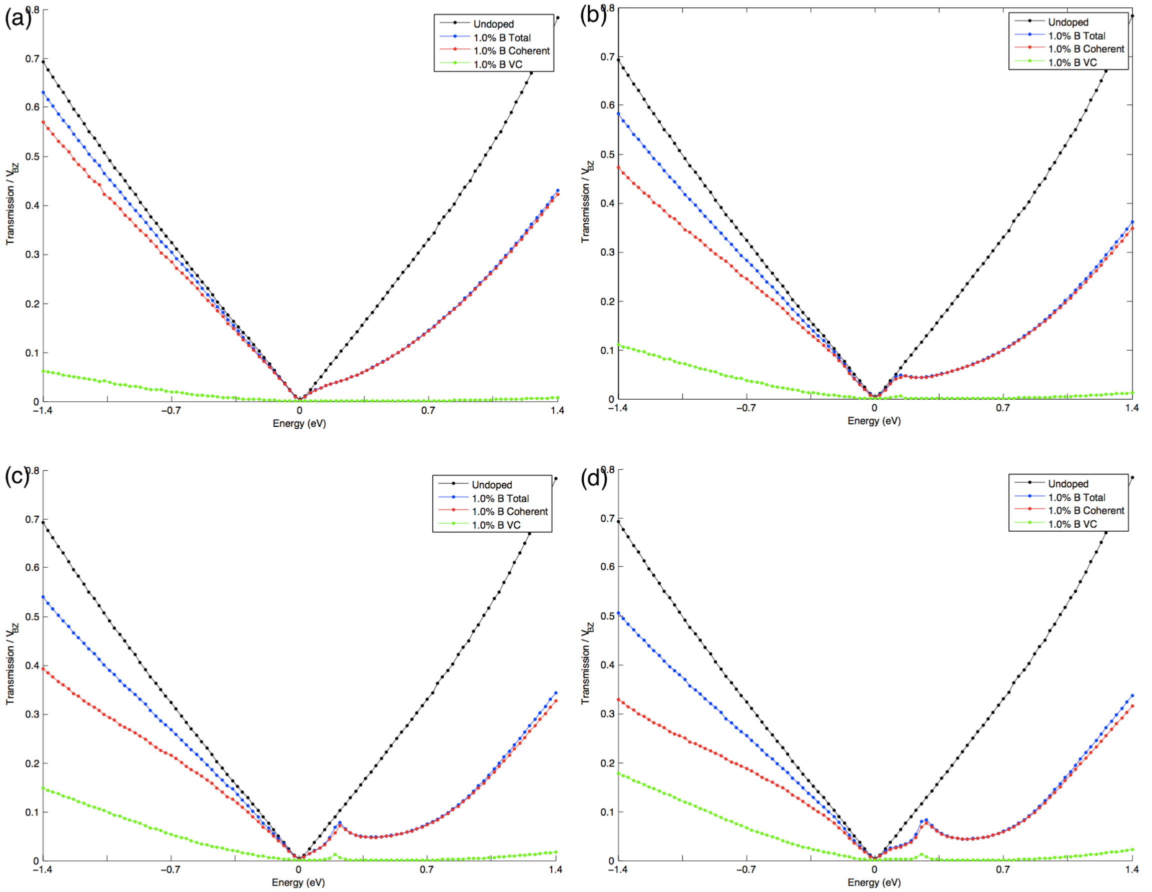

Figure 5.16: Transmission coefficient $T(E)$ versus electron energy for a graphene device with 1% boron impurities. (a) 1.22 nm (b) 2.45 nm (c) 3.68 nm (d) 4.9 nm. The black curve is the transmission for perfect graphene without any impurity, for comparison purposes. The blue curve is the total transmission with 1% impurity. The red curve is the coherent part of the transmission (the first term of Eq. (4.3.8); and the green curve is the vertex contribution which describes the diffusive scattering, namely the second term of Eq. (4.3.8).

5.4 Graphene P-N junctions

In this Section, we investigate what happens if we dope one half of the device with B and the other half with N, making a molecular P-N junction out of the doped graphene. Results for DOS and transmission coefficient are shown in Figs. 5.17 and 5.18, respectively. Very interestingly, we observe that when the graphene is n-doped on one side and p-doped on the other side, the DOS behaviours of either type of impurity, namely Figs. 5.8(b) and 5.9(b), are almost combined in additive ways as shown in Fig. 5.17. Such an additive effect also shows up in the $T(E)$ curve of Fig. 5.18, such that $T(E)$ curves have peaks on both sides of the Fermi energy. Fig. 5.19 plots the electrostatic potential of the graphene P-N junction which shows a clear band bending at the junction, mimicking what happens in semiconductor P-N junctions.

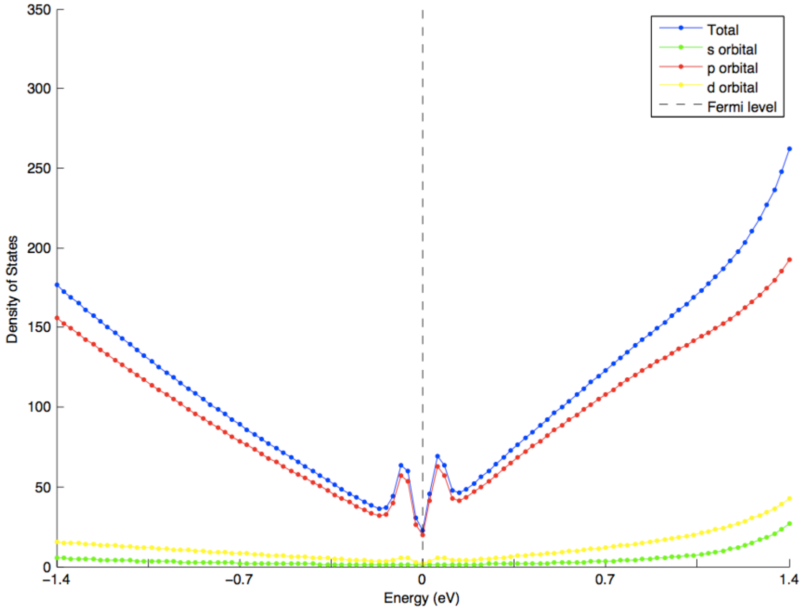

Figure 5.17: Total density of states of a p-n junction constructed by doping one half of the device with 1% boron and the other half with 1% nitrogen.

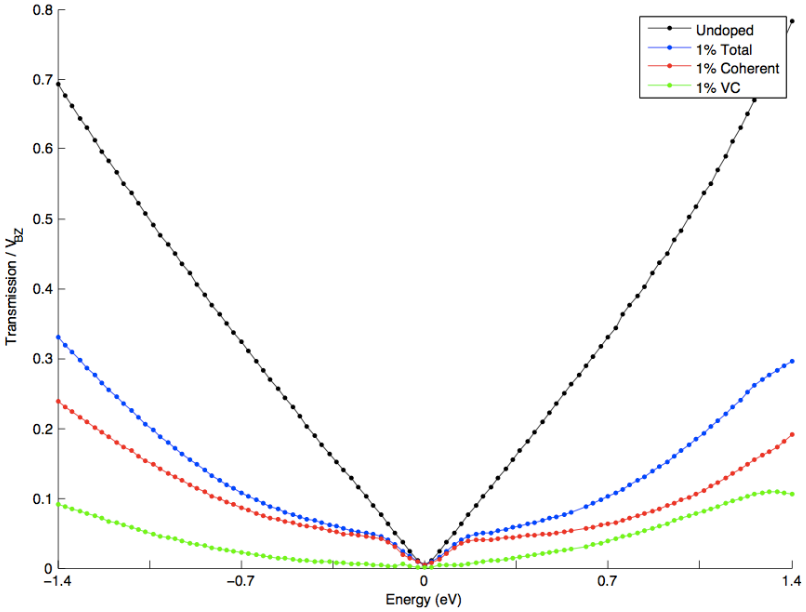

Figure 5.18: $T(E)$ of a 4.9 nm graphene p-n junction doped with 1% boron on one half and 1% nitrogen on the other half.

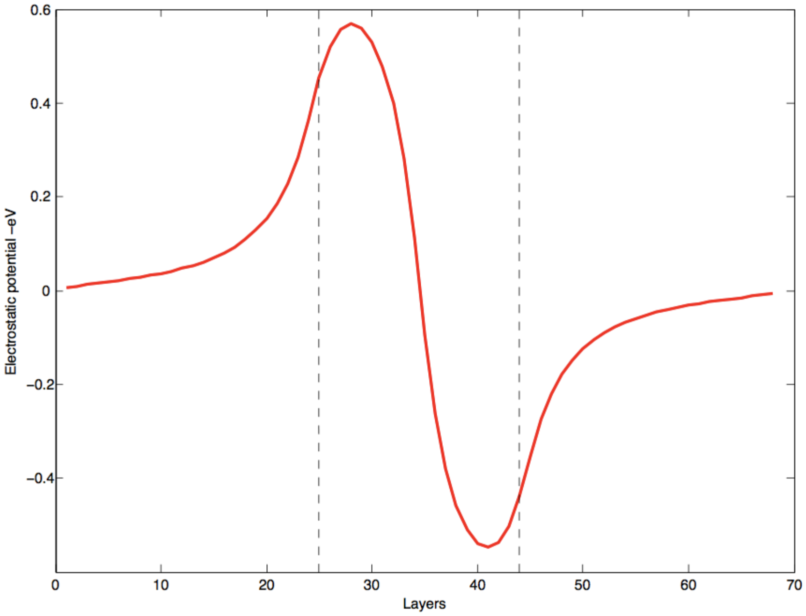

Figure 5.19: The electrostatic potential of a 10 layer 1% B - 10 layer 1% N P-N junction. The region between the dashed lines is the region where the doping takes place. The outer regions serve as screening buffers.

5.5 Summary

We have carried out atomic first principles calculation on quantum transport properties through graphene nano-devices with substitutional disorder. We have found a rather good ASA representation of the empty spheres that allows us to investigate graphene using the LMTO method of NEGF-DFT. To the best of the author's knowledge, this is the first time that ASA has been figured out for single layer graphene.

Our first principle calculation vividly shows the effects of boron and nitrogen impurities to the density of states, electrostatic potential and transmission coefficients. Doping either adds additional free electrons or holes to the system. This causes not only a shift in the Fermi energy, the impurities also act as scattering centers and provide diffusive scattering signified by the prominent contributions from the vertex correction part of the transmission coefficient, as shown in Figs. 5.13 and 5.14.

We have seen that the differences between boron and nitrogen doping arise almost purely from the fact that some charge is added or removed by the impurities. Looking at the window close to the Fermi energy, we observe that these effects are almost exactly mirrored from boron to nitrogen, suggesting that the doping effects are indeed electronic in nature. When we dope one side with B atoms and the other side with N atoms, we can see from the potential plot of Fig. 5.19 that this device acts as a P-N junction. Looking at the density of states and the transmission, both B and N were contributing and the total effect is almost additive from either species.

These results therefore suggest that substitutional disorder plays a significant role in the transport properties of graphene. These effects might not be a bad thing, considering how doping is used in semiconductors to achieve the desired properties. Using doping in graphene, one could alter its electronic properties significantly as our calculations showed.

6

Conclusions

This thesis starts and ends with graphene. Single layer graphene has only been systematically produced in the past few years but has already earned a Nobel Prize of Physics for its discoverers exemplifying the importance and impact of this material. With the huge amount of research conducted on graphene, it is likely that many serious practical applications will be discovered. Before that happens, however, considerable advances are still needed in understanding the properties of graphene placed in many different material environments. As it stands now, the author believes that, not only for graphene but also for other materials, it is very important to take realistic situations into account. The theory outlined in this thesis can describe disorder scattering due to substitutional impurities from atomic first prinicples which is highly advantageous for the field of quantum transport modeling.

After a review of basic concepts in electronic theory, a more detailed review of density functional theory was given. Then, we have presented LMTO which is an orbital method of choice to solve the Kohn-Sham equations for very large solid crystals. To study quantum transport which has open devices and transport boundaries as well as external bias voltages, the NEGF-DFT method has been discussed. Extensions of NEGF-DFT to handle substitutional disorder, the CPA and NVC theories have then been introduced and the whole NEGF-CPA-NVC formalism has been integrated into DFT and LMTO-ASA.

We have applied this theory to calculate electronic structure of disordered graphene.

The disorder is taken to be substitutional doping of boron and nitrogen atoms in various concentrations. Through the density of states, it was explained how doping affected transmission such as the transmission peaks that were direct results of the particular form of the total densities of states. It was also seen that the vertex correction term describing the diffusive scattering played a large role in determining the transmission, accounting for most of the impurity contributions. Varying the concentration and the device length allowed us to see their influences on the transport properties, generally being that the more impurities there are, both absolutely and relatively, the more impurity scattering will happen and the more the system will take on the electronic properties of the impurity. Comparing the effects of boron and nitrogen also shows very interesting observations. Since electronically, the effects of boron and nitrogen are each other's opposites, it was very interesting to observe that their contributions close to the Fermi energy were indeed almost exactly mirrored. Finally, we studied the system where one half of the device was doped with boron and the other half was doped with nitrogen. Electrostatically, this created a P-N junction. Most interestingly, the co-doping gives results are almost additive, at least for the P-N junction cases.

While we have made good progress in understanding disorder effects to graphene transport, there are many further investigations to carry out. An interesting problem is to connect graphene to a metal or a semiconductor and study its electronic and quantum transport properties, as in realistic situations the device will always be connected to metal electrodes and most likely, hybridize with semiconductor materials. Another very interesting system is bilayer graphene, which has very promising and even peculiar electronic properties. The disorder scattering physics that has been investigated in this thesis could appear in many different systems. The author would like to express his hope and wish that in the future, this thesis could be written on a graphene based computer.

BIBLIOGRAPHY

[1] A. K. Geim and K. S. Novoselov. The rise of graphene. *Nature Materials*, 6:183–191, 2007.

[2] A. H. Castro Neto, F. Guinea, N. M. R. Peres, K. S. Novoselov, and A. K. Geim. The electronic properties of graphene. *Rev. Mod. Phys.*, 81(1):109–162, 2009.

[3] http://en.wikipedia.org/wiki/brillouin_zone.

[4] http://www.ugrad.physics.mcgill.ca/wiki/index.php/phys-558_solid_state_physics.

[5] http://en.wikipedia.org/wiki/density_functional_theory.

[6] P. A. Khomyakov, G. Giovannetti, P. C. Rusu, G. Brocks, J. van den Brink, and P. J. Kelly. First-principles study of the interaction and charge transfer between graphene and metals. *Phys. Rev. B*, 79(19):195425, 2009.

[7] K. S. Novoselov, A. K. Geim, S. V. Morozov, D. Jiang, M. I. Katsnelson, I. V. Grigorieva, S. V. Dubonos, and A. A. Firsov. Two-dimensional gas of massless dirac fermions in graphene. *Nature*, 438(7065):197–200, 2005.

[8] K. S. Novoselov, D. Jiang, F. Schedin, T. J. Booth, V. V. Khotkevich, S. V. Morozov, and A. K. Geim. Two-dimensional atomic crystals. *Proceedings of the National Academy of Sciences of the United States of America*, 102(30):10451–10453, 2005.

[9] P. R. Wallace. The band theory of graphite. *Phys. Rev.*, 71(9):622–634, 1947.

[10] J. C. Slonczewski and P. R. Weiss. Band structure of graphite. *Phys. Rev.*, 109(2):272–279, 1958.

[11] R. E. Peierls. Quelques propriétés typiques des corpss solides. *Ann. I. H. Poincaré*, 5:177–222, 1935.

[12] L. D. Landau. Zur theorie der phasenumwandlungen ii. *Phys. Z. Sowjetunion*, 11:26–35, 1937.

[13] S. Das Sarma, Shaffique Adam, E. H. Hwang, and Enrico Rossi. Electronic transport in two-dimensional graphene. *Rev. Mod. Phys.*, 83(2):407–470, 2011.

[14] J. E. Padilha, R. B. Pontes, A. J. R. da Silva, and A. Fazzio. Ixv curves of boron and nitrogen doping zigzag graphene nanoribbons. *International Journal of Quantum Chemistry*, 111(7-8):1379–1386, 2011.

[15] K. Carva, B. Sanyal, J. Fransson, and O. Eriksson. Defect-controlled electronic transport in single, bilayer, and n-doped graphene: Theory. *Phys. Rev. B*, 81:245405, 2010.

[16] Youqi Ke, Ke Xia, and Hong Guo. Disorder scattering in magnetic tunnel junctions: Theory of nonequilibrium vertex correction. *Phys. Rev. Lett.*, 100(16):166805, 2008.

[17] Youqi Ke. *Theory of Non-equilibrium Vertex Correction.* PhD thesis, McGill University, 2010.

[18] Zi Wang, Youqi Ke, Jesse Maassen, and Hong Guo. Electronic transport through disordered graphene from first principles. In preparation, to be submitted 2011.

[19] Michael P. Marder. *Condensed Matter Physics.* Wiley-Interscience, 2000.

[20] Henrik Bruus and Karsten Flensberg. *Many-Body Quantum Theory in Condensed Matter Physics: An Introduction.* Oxford University Press, 2004.

[21] Robert G. Parr and Weitao Yang. *Density-functional theory of atoms and molecules.* Oxford University Press US, 1994.

[22] P. Hohenberg and W. Kohn. Inhomogeneous electron gas. *Phys. Rev.*, 136(3B):B864–B871, 1964.

[23] W. Kohn and L. J. Sham. Self-consistent equations including exchange and correlation effects. *Phys. Rev.*, 140(4A):A1133–A1138, 1965.

[24] Mel Levy. Universal variational functionals of electron densities, first-order density matrices, and natural spin-orbitals and solution of the v-representability problem. *Proceedings of the National Academy of Sciences*, 76(12):6062–6065, 1979.

[25] L. H. Thomas. The calculation of atomic fields. *Proc. Cambridge Phil. Soc.*, 23(05):542–548, 1927.

[26] E. Fermi. Un metodo statistico per la determinazione di alcune priopretà dell'atomo. *Rend. Accad. Naz. Lincei*, 6:602–607, 1927.

[27] Peter Elliott, Filipp Furche, and Kieron Burke. *Excited States from Time-Dependent Density Functional Theory*, pages 91–165. John Wiley & Sons, Inc., 2009.

[28] U. von Barth and L. Hedin. A local exchange-correlation potential for the spin polarized case. i. *Journal of Physics C: Solid State Physics*, 5(13):1629, 1972.

[29] Hans L. Skriver. *The LMTO Method: Muffin-Tin Orbitals and Electronic Structure.* Springer-Verlag, 1984.

[30] I. Turek, V. Drchal, J. Kudrnovský, M. Šob, and P. Weinberger. *Electronic Structure of Disordered Alloys, Surfaces and Interfaces.* Kluwer Academic Publishers, 1997.

[31] O. Krogh Andersen. Linear methods in band theory. *Phys. Rev. B*, 12(8):3060–3083, 1975.

[32] O. K. Andersen and O. Jepsen. Explicit, first-principles tight-binding theory. *Phys. Rev. Lett.*, 53(27):2571–2574, 1984.

[33] Youqi Ke, Ferdows Zahid, V. Timoshevskii, Ke Xia, D. Gall, and Hong Guo. Resistivity of thin Cu films with surface roughness. *Phys. Rev. B*, 79(15):155406, 2009.

[34] Ferdows Zahid, Youqi Ke, Daniel Gall, and Hong Guo. Resistivity of thin Cu films coated with Ta, Ti, Ru, Al, and Pd barrier layers from first principles. *Phys. Rev. B*, 81(4):045406, Jan 2010.

[35] V. Eyert. A comparative study on methods for convergence acceleration of iterative vector sequences. *Journal of Computational Physics*, 124(2):271 – 285, 1996.

[36] D. Glotzel, B. Segall, and O. K. Andersen. Self-consistent electronic structure of si, ge and diamond by the lmto-asa method. *Solid State Communications*, 36(5):403 – 406, 1980.

[37] L. V. Keldysh. Diagram technique for nonequilibrium processes. *Zh. Eksp. Teor. Fiz.*, 47:1515–1527, 1964.

[38] Jeremy Taylor, Hong Guo, and Jian Wang. Ab initio modeling of quantum transport properties of molecular electronic devices. *Phys. Rev. B*, 63(24):245407, 2001.

[39] Supriyo Datta. *Electronic Transport in Mesoscopic Systems*. Cambridge University Press, 1997.

[40] Antti-Pekka Jauho, Ned S. Wingreen, and Yigal Meir. Time-dependent transport in interacting and noninteracting resonant-tunneling systems. *Phys. Rev. B*, 50(8):5528–5544, 1994.

[41] Jian Wang and Hong Guo. Relation between nonequilibrium green's function and lippmann-schwinger formalism in the first-principles quantum transport theory. *Phys. Rev. B*, 79(4):045119, 2009.

[42] Supriyo Datta. *Quantum Transport: Atom to Transistor*. Cambridge University Press, 2005.

[43] Sergey V. Faleev, Fran çois Léonard, Derek A. Stewart, and Mark van Schilfgaarde. Ab initio tight-binding lmto method for nonequilibrium electron transport in nanosystems. *Phys. Rev. B*, 71(19):195422, 2005.

[44] G. Stefanucci and C.-O. Almbladh. Time-dependent quantum transport: An exact formulation based on tddft. *EPL (Europhysics Letters)*, 67(1):14, 2004.

[45] Xiao Zheng, Fan Wang, Chi Yung Yam, Yan Mo, and GuanHua Chen. Time-dependent density-functional theory for open systems. *Phys. Rev. B*, 75(19):195127, 2007.

[46] Paul Soven. Coherent-potential model of substitutional disordered alloys. *Phys. Rev.*, 156(3):809–813, 1967.

[47] D. W. Taylor. Vibrational properties of imperfect crystals with large defect concentrations. *Phys. Rev.*, 156(3):1017–1029, 1967.

[48] B. Velický, S. Kirkpatrick, and H. Ehrenreich. Single-site approximations in the electronic theory of simple binary alloys. *Phys. Rev.*, 175(3):747–766, 1968.

[49] Youqi Ke, Ke Xia, and Hong Guo. Oxygen-vacancy-induced diffusive scattering in Fe/MgO/Fe magnetic tunnel junctions. *Phys. Rev. Lett.*, 105(23):236801, 2010.

[50] Mathieu César, Youqi Ke, Wei Ji, Hong Guo, and Zetian Mi. Band gap of $\mathrm{In}_x\mathrm{Ga}_{1-x}\mathrm{N}$: A first principles analysis. *Applied Physics Letters*, 98(20):202107, 2011.

[51] M P Lopez Sancho, J M Lopez Sancho, and J Rubio. Quick iterative scheme for the calculation of transfer matrices: application to mo (100). *Journal of Physics F: Metal Physics*, 14(5):1205, 1984.

[52] V. M. Karpan, P. A. Khomyakov, A. A. Starikov, G. Giovannetti, M. Zwierzycki, M. Talanana, G. Brocks, J. van den Brink, and P. J. Kelly. Theoretical prediction of perfect spin filtering at interfaces between close-packed surfaces of Ni or Co and graphite or graphene. *Phys. Rev. B*, 78(19):195419, 2008.

[53] Jesse Maassen, Wei Ji, and Hong Guo. First principles study of electronic transport through a Cu(111)|graphene junction. *Applied Physics Letters*, 97(14):142105, 2010.

[54] Aurélien Lherbier, X. Blase, Yann-Michel Niquet, Francois Triozon, and Stephan Roche. Charge transport in chemically doped 2d graphene. *Phys. Rev. Lett.*, 101(3):036808, 2008.

[55] M. Terrones, A. Jorio, M. Endo, A.M. Rao, Y.A. Kim, T. Hayashi, H. Terrones, J.-C. Charlier, G. Dresselhaus, and M.S. Dresselhaus. New direction in nanotube science. *Materials Today*, 7(10):30 – 45, 2004.